Journal of Thermal Science

https://doi.org/10.1007/s11630-024-1934-z

Application of Response Surface Methodology for Analysing and Optimizing the Finned Solar Air Heater

Vineet SINGH[1*], Vinod Singh YADAV[2], Vaibhav TRIVEDI[1], Manoj KUMAR[1], Niraj KUMAR[3]

1. Department of Mechanical Engineering, School of Engineering & Technology, IFTM University, Moradabad, Uttar Pradesh, India
2. Department of Mechanical Engineering, NIT, Uttarakhand, Pauri, Uttarakhand, India
3. Department of Electronics and Communication Engineering, Jaypee Institute of Information Technology, Noida, Uttar Pradesh 201309, India

Abstract: In this research paper, a solar air heater with triangular fins has been experimentally analysed and optimized. Initially, an experimental set-up of a solar air heater having triangular fins has been developed at the location of 28.10°N, 78.23°E. The heat transfer rate through fins and fins efficiency has been determined by the Finite Difference Method model equations. The experimental data and modeled data of response parameters have been optimized in MINITAB-17 software by the Response Surface Methodology tool. For creating the response surface design, three input parameters have been selected namely solar intensity, Reynolds number, and fin base-to-height ratio. The range of solar intensity, Reynolds number, and fin base-to-height ratio is 600 to 1000 W/m^2, 4000 to 6000, and 0.4 to 0.8 respectively. The response surface design has been analyzed by calculating the outlet temperature, friction factor, Nusselt number, fin efficiency, thermal performance factor, and exergy efficiency. The optimum settings of input parameters: solar intensity is 1000 W/m^2; Reynolds number is 4969.7, and the fin base to height ratio is 0.6060, on which these response: namely outlet temperature of 92.531°C, friction factor of 0.2350, Nusselt number of 127.761, thermal efficiency of 50.836%, thermal performance factor of 1.4947, and exergy efficiency of 8.762%.

Keywords: solar air heater; optimization; fins; exergy; response surface methodology; air

1. Introduction

From an energy point of view, solar energy will play an important role for full filling the world's energy demand without any pollution. One of the most important applications of solar energy is to heat the atmospheric air for warming rooms, crop drying, seasoning the wood, and heating the oil in the refineries. The air is heated in the Solar Air Heater (SAH) by flowing the air over the surface of the Absorber Plate (AP). The performance of SAH depends on the outlet temperature of the air and the mass flow rate of the air. The heat transfer to the air depends on the heat transfer coefficient between the AP and the air. The main aim of the SAH is to increase the heat transfer coefficient by increasing the roughness over the surface [1]. The enhancement in heat transfer coefficient also leads to the increase in friction factor and pressure drop. So, the SAH gives the maximum

---

Received: Mar 20, 2023 AE: YAN Suying Corresponding author: Vineet SINGH E-mail: vineetpsh@gmail.com

Nomenclature			
C_P	Specific heat of air/J·(kg·K)$^{-1}$	η_{SAH}	Efficiency of solar air heater/%
Ex_{IN}	Exergy entering in the solar air heater	θ	Tilt angle
Ex_{OUT}	Exergy leak in the atmosphere	ρ	Density of air/kg·m^{-3}
Ex_{DEST}	Exergy destruction due to irreversibility in the system	σ	Stefan Boltz's man constant, 5.67×10^{-8} W/(m^2·K^4)
h_{r}	Radiation heat transfer coefficient/W·(m^2·K)$^{-1}$	Ψ	Exergetic efficiency of SAH/%
h_{c}	Heat transfer coefficient/W·(m^2·K)$^{-1}$	**Acronyms**	
k	Boltzmann constant	AP	Absorber Plate
Nu_{L}	Nusselt number	CFD	Computational Fluid Dynamics
Ra_{L}	Rayleigh number	FF	Friction Factor
S_{F}	Solar Intensity/W·m^{-2}	HT	Heat Transfer
T_{a}	Atmospheric temperature/K	HTC	Heat Transfer Coefficient
T_{P}	AP temperature/K	MFR	Mass Flow rate
T_{sky}	Sky temperature/K	PCM	Phase Change material
T_{sun}	Sun temperature/K	PD	Pressure Drop
V	Velocity of air flow over the SAH cover plate/m·s^{-1}	RN	Reynolds Number
y	Inaccuracy in measurement	RSM	Response Surface Methodology
Symbols		SAH	Solar Air Heater
α	Absorptivity or absorption coefficient	SSAH	Simple Solar Air Heater
ε	Emissivity of solar panel material	SSAHF	Simple Solar Air Heater with Fins
η	Efficiency of the fin/%		

performance at the optimum mass flow rate and the optimum hydraulic parameters. The optimum Reynolds number has been determined at 12 000 at which the increment in Nusselt number and friction factor obtained to be 1.81 and 3.13 times the initial values [2]. The main interest in SAH is to reduce friction losses and increase heat transfer so that exergy efficiency should be maximized and exergy destruction minimized [3].

The three sides' roughness of SAH has been optimized by RSM and MOPSO algorithms. The values of output parameters like Nusselt number and thermal efficiency are determined to be 65%–80% and 63%–75% at the optimum value of Reynolds number of 12 000–13 000 [4]. The quarter circular ribs have been used for increasing the heat transfer rate of the SAH. The velocity, pressure, and temperature field have been determined by the CFD simulation software 18. The optimum hydraulic circular pitch was obtained to be 7.18. The non-linear regression analysis has been performed and formed the equation of the Nusselt number and the friction factor in terms of input variables [5]. The relative toughness can be enhanced by providing obstacle length and the obstacle angle. The energy and exergy efficiency equations can be developed in terms of the optimum obstacle length and obstacle angle [6].

Numerical and experimental studies have been conducted on staggered arc ribs at varying mass flow rates. The proposed system increases the friction factor and Nusselt number by 2.57 and 3.16 times as compared to smooth SAH. The closed ribs configuration increases the 1.22 times Nusselt number as compared to the open ribs configuration [7]. The SAH works only when solar energy is available in the atmosphere. This is the big drawback of SAH, so the PCM material is used below the AP and will be analyzed by ANSYS CFD [8]. The circular ribs used above the AP for increasing the roughness of air and the turbulence characteristics of the air have been analyzed in the ANSYS CFD v16. The Reynolds number varies between 3800–18 000 and the pitch ratio varies between 12–25 [9]. In a research study, the air does not pass over the AP but passes through the glass vacuum tube. The increase in solar flux from 675 W/m^2 to 835 W/m^2 and then SAH efficiency increased from 70.22% to 77.28%. It is also concluded that the increase in atmospheric temperature increases the efficiency of SAH [10]. The arc-type fins are used over the AP for increasing the turbulence and the heat transfer coefficient. The model has been designed at varying the arc rib height ratio and determined the optimum geometry. The performance parameters like the outlet temperature, Nusselt number, fin efficiency, and heat removal factor have been determined at varying flow rates. It is finally concluded that the variable arc rib fins have a higher heat transfer than the fixed rib fins SAH

[11]. The arc-shaped ribs have been provided at the inner side of the AP. The optimization of the SAH has been done by the RSM and 2nd order polynomial has been formed, which provides the data for the Nusselt number and the friction factor. The RSM-optimized results of the Nusselt number and friction factor have been validated with experimental results of 6% accuracy [12]. The surface roughness plays a very important role in increasing the turbulence between the AP and the air. In one of the research studies, staggered cuboidal shape baffles have been used above the AP. The investigation of the SAH has been done by the CFD analyses and then optimized the system by the Taguchi method. The Taguchi method has been used for determining the optimum geometry of the baffles. The numerical results reveal that the new optimized system works better than the simple SAH. It is finally concluded that the relative baffles' height and the relative roughness pitch are highly affected by the heat transfer and the friction factor [13]. The combined CFD and RSM techniques have been used for determining the heat transfer and pressure drop over the absorber plate when inclined fins are used over the AP. The optimization results have been carried out by varying fin length in the range of 1.5 mm to 2.5 mm; the inclination of the fins varies in the range of 30°–60°, the pitch range from 15–25 mm, and the Reynolds number in the range of 4000–24 000. The optimum results of the length of the fins were found to be 1.52 mm, optimum angle of 49°, and optimum Reynolds number of 18 243.5 [14]. A finned SAH has been used in the food drying and optimized based on experimental data. The RSM is used for optimizing the system based on the length-to-width (L/W) ratio, the height of the air duct, and the number of fins. The optimized system increases the thermal efficiency by 15.76% [15]. The double pass SAH having porous medium and without porous medium has been investigated by natural and forced convection. The experimental study have been conducted during the winter season. The higher efficiency has been getting when the system was operated at natural convection as compared to forced convection. In natural convection mode, the maximum efficiency of both SAH has been obtained to be 87% and 82% but on the other hand in forced convection mode maximum efficiency in forced convection has been obtained to be 81% and 67% [16]. A tubular heat exchanger has been compared with the SSAH at energy, exergy and economic level and it was found that the performance of tubular heat exchanger is better than the SSAH. The pumping power required for flowing the air in the tubular pipe is less than the SSAH [17].

A very new unique technique has been used for improving the performance of SAH by making multiple holes over the AP. The multiple holes increase the turbulence better than the roughened surface at minimum power loss. The system has been optimized by RSM at several input variables like hole diameter, pitch of the hole, length of SAH, and varying mass flow rate. The results show that the optimized mass flow rate, jet diameter, pitch, and length of SAH are 0.013 86 kg/s, 0.0046 m, 0.051 08 m, and 15 108 m respectively [18].

The SAH design is very simple and less costly as compared to other air heating techniques but the main drawback is its heating capacity and efficiency. So a V groove design has been proposed which increases the efficiency and heat transfer capacity to the air. The two types of cover are also used in SAH: one is a simple cover and the other is a fresnel lens cover. It is finally concluded that the fresnel cover has higher efficiency and heat transfer characteristics as compared to SSAH [19]. Nanofluid plays an important role in heat transfer in flowing liquids in the tubes. A photo voltaic thermal cooling system has been designed and the cooling of the solar panel is provided by the nao fluids. ANSYS software has been used to analyze the effect of the Reynolds number, nanofluid phase concentration, and groove pitch. The optimum phase concentration, Reynolds number, and groove pitch were selected to be 1%, with Re=2000, and S=0.25 [20].

An SSAH has been having tin cans used for creating turbulence in the air flow duct. The system has been analyzed by COMSOL software for visualizing the velocity, pressure, and temperature field. Three different models have been designed and compared based on energy and exergy efficiency [21].

The artificial roughness of the SAH absorber plate has been increased by the L-shaped ribs in the reverse mode. The system has been analyzed experimentally and numerically and compared to each other. The results have been compared at varying Reynolds numbers at the solar flux of 1000 W/m^2 [22].

A review of SAH has been published which contains the different models used in CFD analyses. The model effectiveness and the mesh quality also play an important role in CFD simulation results that have been represented in Ref. [23]. Waste material recycling not only decreases the cost of the material but also reduces the pollution in the environment. A study has been conducted for using the tubular waste heat pipe in SAH. The analysis has been done numerically and experimentally and validated the results. The experiment has been conducted at two tilt angles 90° and 32° at varying flow rates [24].

The roughness of SAH has been increased by fixing the transverse wire over the surface of AP and the system investigated by the CFD ANSYS software. The effect of wire diameter on heat transfer, velocity, and pressure distribution has been analyzed experimentally and numerically. The selected input variables were the

Reynolds number, relative roughness pitch, and relative roughness height [25].

The channel depth gives an immense effect on the turbulence and heat transfer to the air. So the channel depth variation on the turbulence and heat transfer have been analyzed by the CFD software. Based on the performance of SAH the optimum depth of the channel was 10 mm [26].

The very interesting curved SAH is designed with grooves formed over the surface of AP. The system has been investigated numerically (CFD software) and validated with the previous study conducted by Singh P.A. et al. (2022). It is finally concluded that the vortex near the surface of SAH increases the Nusselt number by a significant amount [27].

Table 1 shows the various design of the solar air heater which have been previously used for improving the heat transfer efficiency and performance of the solar air heater. The increasing roughness of the absorber plate improves the heat transfer, but simultaneously due to the enhancement of pressure drop, it shows a negative effect on the exergetic efficiency and the net efficiency of the SAH [30]. So, in every design of solar heater, the optimization of geometry is an important part. Table 2 represents the use of RSM for designing the solar air heater.

Table 1 Summary of experimental analyses on SAH

NO.	Proposed Geometry of SAH	Results of various peromance parameters	Year of Publication	Author Details
1	Inclined vortex plate over the absorber plate in a SAH.	Energy and Exergy efficiency, Nusselt Number, Friction factor	2019	(H. Xiao et al.) [2]
2	S-shaped ribs on the surface of the AP of SAH.	Nusselt Number, friction factor, and flow visualization by the CFD	2021	(S.K. Bauri and A.K. Prasad) [1]
3	Quarter circular ribs over the surface of SAH.	Heat transfer and pressure drop calculation on the surface of SAH at varying Reynolds Numbers, relative roughness pitch, and relative roughness height.	2021	(Y. Mahanand and J.R. Senapati) [28]
4	Obstacle fixed over the surface of AP.	Different obstacle lengths, obstacle angles, and Reynolds Numbers have to be determined by the energy and exergy of the SAH.	2017	(A. Acır et al.) [6]
5	Broken arc and staggered ribs were used over the surface of AP for increasing the heat transfer rate.	The performance of SAH has been determined by the mass flow rate and geometric parameters. The main geometric parameters have been selected to be staggered rib position, roughness pitch, gap width, gap position, Roughness height arc angle, staggered rib piece size, and the Reynolds number.	2021	(R.S. Gill et al.) [7]
6	Phase change material is used as energy storage in SAH. The PCM material was fixed at the back of the AP.	The system has been optimized at varying mass flow rates, paraffin thermal conductivity, and amount of paraffin.	2017	(R. Moradi et al.) [8]
7	Use circular ribbed roughened SAH under investigation.	The Nusselt number and friction factor have been determined by the varying Reynolds number and pitch of the circular ribs.	2021	(A.S. Yadav et al.) [29]
8	Fixed a circular wire over the surface of SAH.	The heat transfer and pressure drop have been determined by varying the mass flow rate and diameter of the wire.	2013	(A.S. Yadav and J.L. Bhagoria) [25]
9	A curved solar air heater design was investigated.	The Nusselt number, friction factor, outlet temperature, efficiency, and exergy have been calculated.	2018	(Ajeet Pratap Singh and O.P. Singh) [27]
10	L-shaped ribs fixed over the surface of AP.	The thermal performance of SAH has been calculated under varying flow and geometric conditions.	2016	(Vipin G. Gawande et al.) [22]
11	A grooved channel shape was created over the AP.	The optimum channel depth has been determined based on the performance of SAH.	2010	(Wie Su et al.) [26]
12	Recycled aluminum bear cans have been used in the duct of SAH.	The performance of SAH has been determined based on parallel and counter flow configuration.	2019	(Moustafa Al Damouk et al.) [21]
13	Staggered cuboidal shape baffles have been used to increase turbulence.	The Taguchi method has been used to optimize the baffles' roughness height and baffles' roughness pitch.	2021	(G. Sureandhar et al.) [13]
14	Inclined fins with varying sizes and inclination angles have been investigated.	CFD and RSM both combined techniques were used for flow visualization and optimizing the performance of SAH based on fins length and inclination angle of fins.	2019	(B. S. Qader et al.) [14]

Table 2 Summary of optimization technique RSM in various design of solar air heaters

No.	Input variables	Response Parameters	Optimization technique	Year of Publication	Authors
1	Mass flow rate Recycling ratio Channel Depth	Thermal efficiency Thermal hydraulic efficiency Outlet air temperature Useful power gain	RSM	2014	(S. Singh and P.Dhiman) [31]
2	Length of SAH Flow rate of air Stream wise pitch (*X*) Span wise pitch (*Y*) Jet diameter	Thermal hydraulic efficiency	RSM	2022	(M. M. Matheswaran et al.) [18]
3	Roughness parameters Height Longitudinal pitch Transverse pitch	Thermohydraulic parametr is 1.20	RSM	2021	(L. N. Azadani and N. Gharouni) [32]
4	Time Solar insolation	Relative Humidity Radiation due to natural convection	RSM	2022	(V. B. Huddar et al.) [33]
5	Length of fin Different slant angle Different pitch Reynolds Number	Nusselt Number Friction Factor THPP	RSM	2019	(B. S. Qader et al.) [14]

The solar air heater performance mainly depends on the solar intensity, Reynolds Number, and roughness of the surface of the absorber plate and these parameters are considered as main input parameters. In the present study, the main objective is to optimize the input variables so that the performance of the solar air heater is the maximum. For that, triangular fins have been fixed over the surface of the absorber plate to enhance the turbulence and heat transfer rates. Although, fins enhances the heat trasfer and turbulence but siultaneously increase the pressure drop. The inceasing pressure drop enhance the blower power which will effect the net effficiency and exergetic efficiency. So that fin geometry must be optimized to enhance the performance. The optimization work has been completed in Minitab 17 software.

2. Methodology Adopted

The above literature review proposed the various design of the SAH and in all designs the authors tried to improve the heat transfer coefficient and minimize the friction factor since roughness enhance the HTC but also enhance the pressure drop simultaneously. So, it is necessary to optimize the geometry of the SAH at which the HTC is maximum and the Friction factor (FF) is minimum. In this research paper, triangular fins have been produced over the absorber plate and analyzed experimentally and optimized. For optimizing the outlet temperature, friction factor, Nusselt Number, efficiency, TPF, and exergy efficiency, Response Surface Methodology (RSM) is used. The selected input variables are the Solar Intensity, Reynolds Number, and the fin base-to-height ratio of the triangular fins. Based on the range of input variables the Design Of Matrix (DoE) has been created in MINITAB 17 software. The DoE generates the various sets of input variables on which the output parameters are calculated by the experimental and model analysis. Further, the generated data of output variables have been optimized in RSM which gives the optimum values of input variables at which solar air heater gives the maximum performance.

3. Finite Differential Formulation of Triangular Fins

It is very tough to determine the temperature distribution along the triangular fin length analytically. So one-dimensional finite difference technique is used for determining the temperature distribution, actual heat transfer, and fin efficiency. Initially, the fins length has been divided into six nodes and five elements. The geometry of the nodes and elements is shown in Figs. 1–4.

The length of the element depends on the number of nodes, and it is given by the following equation presented in [34].

$$\Delta x = \frac{L}{m-1} \tag{1}$$

where L is the fin length and m is the number of nodes. The 0 node is at the base temperature of the AP. Now the temperatures at nodes 1–5 have been determined by the formulation of five equations. The temperatures at nodes 1–4 have been determined by applying the energy balance at the interior elements of this volume and the temperature of node 5 has been determined by applying the endpoint boundary condition at point 5 [35].

It is assumed that heat transfer occurs at a steady state on all sides of the small element, so as per the energy balance for small elements.

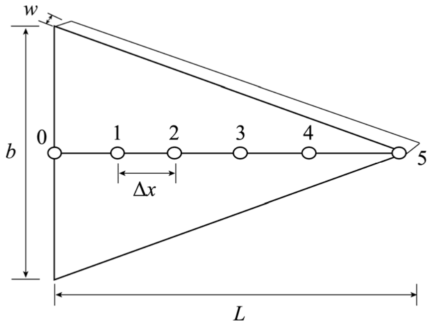

Fig. 1 Geometry of triangular fins with node and element

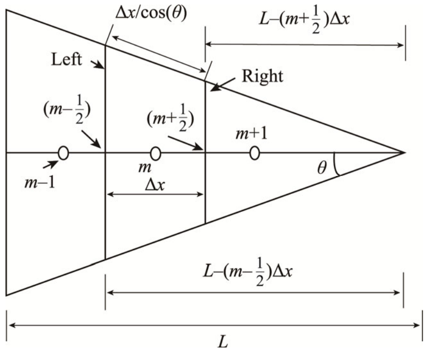

Fig. 2 Location of a small element of length Δx in the volume of triangular fins

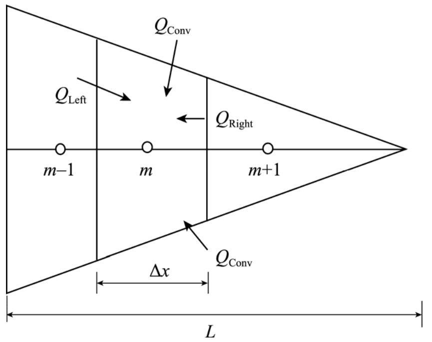

Fig. 3 Heat transfer in the volume of a small element of length Δx

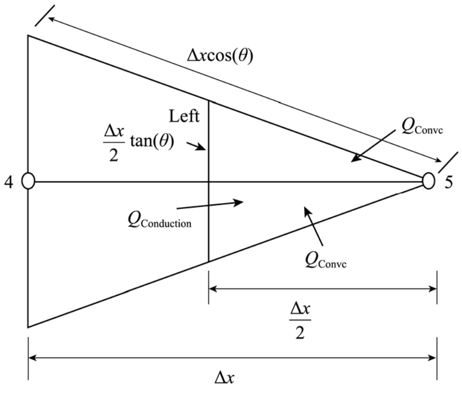

Fig. 4 Heat transfer in the volume of a small element of length Δx in between nodes 4 and 5

$$\frac{kA_{\text{left}}\left(T_{m-1}-T_m\right)}{\Delta x}+\frac{kA_{\text{right}}\left(T_{m+1}-T_m\right)}{\Delta x}+hA_{\text{conv}}\left(T_{\text{atm}}-T_m\right)=0 \tag{2}$$

where k represents the thermal conductivity of the material and h is the heat transfer coefficient. A_{left}, A_{right} and A_{conv} are the areas of the left, right, and convection of the small element. T is temperature. T_{atm} is the atmospheric temperature in kelvin.

These are represented by the following equations [36].

$$A_{\text{left}}=2w\left[L-\left(m-\frac{1}{2}\right)\Delta x\right]\tan\theta \tag{3}$$

$$A_{\text{right}}=2w\left[L-\left(m+\frac{1}{2}\right)\Delta x\right]\tan\theta \tag{4}$$

$$A_{\text{conv}}=2w\Delta x/\cos\theta \tag{5}$$

where w is the thickness of the fins and θ is the vertex angle of the triangular fin.

Now put all the values in Eq. (2):

$$\begin{aligned}&2wk\left[L-\left(m-\frac{1}{2}\right)\Delta x\right]\frac{\tan\theta\left(T_{m-1}-T_m\right)}{\Delta x}\\&+2wk\left[L-\left(m+\frac{1}{2}\right)\Delta x\right]\frac{\tan\theta\left(T_{m+1}-T_m\right)}{\Delta x}\\&+2wh\frac{\Delta x\left(T_{\text{atm}}-T_m\right)}{\cos\theta}=0\end{aligned} \tag{6}$$

$$\begin{aligned}&\left[1-\frac{(m-1/2)\Delta x}{L}\right]\left(T_{m-1}-T_m\right)\\&+\left[1-\frac{(m+1/2)\Delta x}{L}\right]\left(T_{m+1}-T_m\right)\\&+\frac{h(\Delta x)^2\left(T_{\text{atm}}-T_m\right)}{kL\sin\theta}=0\end{aligned} \tag{7}$$

$$\begin{aligned}&\left[1-\left(m-\frac{1}{2}\right)\frac{\Delta x}{L}\right]T_{m-1}\\&-2T_m\left[\left(1-\frac{m\Delta x}{L}\right)-\frac{h(\Delta x)^2}{kL\sin\theta}\right]\\&+\left[1-\left(m+\frac{1}{2}\right)\frac{\Delta x}{L}\right]T_{m+1}=-\frac{h(\Delta x)^2}{kL\sin\theta}\end{aligned} \tag{8}$$

So this is the final model equation that is used to develop the four equations.

Now put m=1, the relation with T_0, T_1, and T_2 is obtained

$$\begin{aligned}&\left(1-\frac{\Delta x}{2L}\right)T_0-2T_1\left[\left(1-\frac{\Delta x}{L}\right)-\frac{h(\Delta x)^2}{kL\sin\theta}\right]\\&+\left(1-\frac{1.5\Delta x}{L}\right)T_2=-\frac{h(\Delta x)^2}{kL\sin\theta}\end{aligned} \tag{9}$$

Now put m=2, the relation with T_1, T_2, and T_3 is obtained

$$\left(1-\frac{3\Delta x}{2L}\right)T_1 - 2T_2\left[\left(1-\frac{2\Delta x}{L}\right)-\frac{h(\Delta x)^2}{kL\sin\theta}\right] + \left(1-\frac{2.5\Delta x}{L}\right)T_3 = -\frac{h(\Delta x)^2}{kL\sin\theta} \tag{10}$$

Now put m=3, the relation with T_2, T_3, and T_4 is obtained

$$\left(1-\frac{5\Delta x}{2L}\right)T_2 - 2T_3\left[\left(1-\frac{3\Delta x}{L}\right)-\frac{h(\Delta x)^2}{kL\sin\theta}\right] + \left(1-\frac{3.5\Delta x}{L}\right)T_4 = -\frac{h(\Delta x)^2}{kL\sin\theta} \tag{11}$$

Now put m=4, the relation with T_3, T_4, and T_5 is obtained

$$\left(1-\frac{7\Delta x}{2L}\right)T_3 - 2T_4\left[\left(1-\frac{4\Delta x}{L}\right)-\frac{h(\Delta x)^2}{kL\sin\theta}\right] + \left(1-\frac{4.5\Delta x}{L}\right)T_5 = -\frac{h(\Delta x)^2}{kL\sin\theta} \tag{12}$$

Eqs. (9)–(12) are used for determining the temperature of T_1, T_2, T_3, and T_4. The temperature T_5 at the end node has been determined by the boundary conditions at the tip of the fin [37].

Now apply the energy balance between nodes 4 and 5 on half of the small element Δx.

$$Q_{\text{conduction}} + Q_{\text{convection}} = 0 \tag{13}$$

$$\frac{kA_{\text{left}}(T_4-T_5)}{\Delta x} + hA_{\text{conv}}(T_{\text{atm}}-T_5) = 0 \tag{14}$$

$$2wk\left(\frac{\Delta x}{2}\right)\frac{\tan\theta(T_4-T_5)}{\Delta x} + 2wh\frac{\Delta x(T_{\text{atm}}-T_5)}{\cos\theta} = 0 \tag{15}$$

$$\frac{k}{2}\tan\theta(T_4-T_5) + \frac{h\Delta x}{\cos\theta}(T_{\text{atm}}-T_5) = 0 \tag{16}$$

Eq. (16) is used to determine the temperature T_5.

The heat transfer Q_{fin} through the fin is determined by the following equation presented in Ref. [34].

$$Q_{\text{fins}} = \sum_{m=0}^{5} hA_{\text{conv}}(T_m - T_{\text{atm}}) \tag{17}$$

$$Q_{\text{fins}} = N_{\text{f}}\left(\frac{hw\Delta x}{\cos\theta}\right) \cdot \left[T_0 + 2(T_1+T_2+T_3+T_4) + T_5 - 10T_{\text{atm}}\right] \tag{18}$$

where N_{f} is the number of fins. The maximum possible heat transfer has been determined if the whole fin is at the base temperature of the copper plate at T_0.

The maximum possible heat transfer is given by

$$Q_{\text{maximum}} = h\frac{2wL}{\cos\theta}(T_0 - T_{\text{atm}}) \tag{19}$$

Now the fin efficiency has been determined by the following equation

$$\eta = \frac{Q_{\text{fins}}}{Q_{\text{maximum}}} \tag{20}$$

4. Velocity Distribution over the AP

The fins are arranged in a staggered fashion on the AP, so air velocity does not remain uniform on the AP. The air velocity becomes the maximum in between the narrow gaps of the triangular fins as shown in Fig. 5. The flow regimes on the AP have been based on the maximum velocity.

In the staggered arrangement of the triangular fins, the maximum velocity $V_{\max}$ has been determined based on Ref. [34].

If $F_{\text{D}} > \frac{F_{\text{T}}+b}{2}$, then the maximum velocity:

$$V_{\max} = \frac{F_{\text{T}}}{F_{\text{T}}-b}V \tag{21}$$

If $F_{\text{D}} < \frac{F_{\text{T}}+b}{2}$, then the maximum velocity has been determined by the following equation [34].

$$V_{\max} = \frac{F_{\text{T}}}{2(F_{\text{D}}-b)}V \tag{22}$$

where V is the free stream velocity; F_{D} is the diagonal pitch; F_{T} is the transverse pitch and F_{L} is the longitudinal pitch.

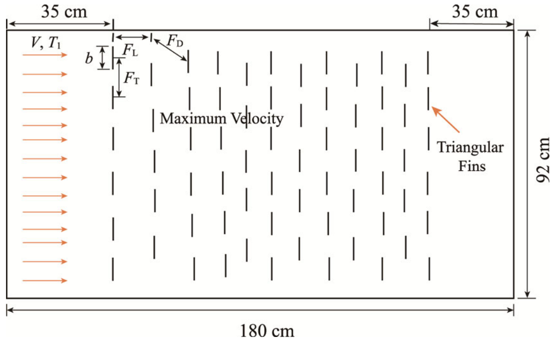

Fig. 5 Geometry of staggered arrangement of the triangular fins

The Reynolds number based on maximum velocity has been determined by

$$Re = \frac{\rho V_{\max} D_{\text{h}}}{\mu} \tag{23}$$

where D_{h} is the hydraulic diameter in m; ρ is the density of air in kg/m^3 and μ is the viscosity of the air in kg/(m·s) at an air temperature of the air. The hydraulic diameter is determined by the following equation presented in Ref. [19].

$$D_{\mathrm{h}}=\frac{2H\sin\left(\theta/2\right)}{1+\sin\left(\theta/2\right)} \tag{24}$$

where H is the height of the fin.

The heat transfer coefficient for staggered arrangement has been determined by the following equations [34].

$$Nu=0.35\left(\frac{F_{\mathrm{T}}}{F_{\mathrm{L}}}\right)^{0.2}Re^{0.6}Pr^{0.36}\left(\frac{Pr}{Pr_{\mathrm{s}}}\right)^{0.25} \tag{25}$$

$$1000<Re<2\times10^{5}$$

$$Nu=0.035\left(\frac{F_{\mathrm{T}}}{F_{\mathrm{L}}}\right)^{0.2}Re^{0.8}Pr^{0.36}\left(\frac{Pr}{Pr_{\mathrm{s}}}\right)^{0.25} \tag{26}$$

$$2\times10^{5}<Re<2\times10^{6}$$

In Eqs. (25) and (26), Re and Pr represent the Reynolds number and Prandlt number respectively. Re and Pr values have been calculated on the arithmetic temperature of air but Pr_{s} is the Prandlt number calculated at the surface temperature of the fins.

The air properties have been selected to be the average temperature of the air

$$T_{\mathrm{average}}=\frac{T_{\mathrm{inlet}}+T_{\mathrm{outlet}}}{2} \tag{27}$$

T_{inlet} and T_{outlet} are the inlet and outlet temperatures of the air in the SAH.

5. Pressure Drop in SAH

When air flows over the AP of the solar air heater, the pressure drop is contributed by both the pressure drag and the shear drag. The pressure drag depends on the shape of the object and shear drag is contributed by the skin coefficient of friction between the air and the AP surface as shown in Fig. 6.

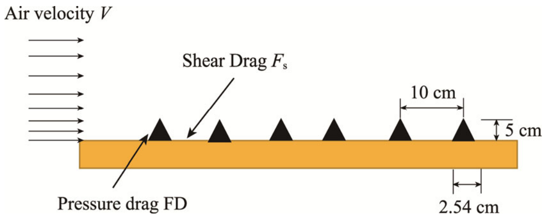

Fig. 6 Schematic view of the AP with triangular fins

So the pressure drop over the AP surface is represented by the following equation [18].

$$P_2-P_1=\left(C_{\mathrm{D}}+C_{\mathrm{f}}\right)\left(\frac{\rho V_{\max}^{2}}{2}\right) \tag{28}$$

The C_{D} is the drag coefficient of the triangular shape fins and C_{f} is the skin friction coefficient of air; it depends on the Reynolds number represented by Eq. (23). The friction coefficient between the air and the flat plate is determined by the following equation [19].

$$C_{\mathrm{f}}=\frac{1.33}{Re^{0.5}}\quad \text{for } Re<2\times10^{5} \text{ (For laminar flow)} \tag{29}$$

$$C_{\mathrm{f}}=\frac{0.074}{Re^{0.2}}\quad \text{for } 5\times10^{5}<Re<10^{7} \text{ (For turbulent flow)} \tag{30}$$

The power consumed by the blower depends on the pressure drop and the discharge flow of the air through the SAH. The following is used for determining the blower power.

$$W_{\mathrm{blower}}=\frac{m_{\mathrm{air}}\Delta P}{\rho_{\mathrm{air}}} \tag{31}$$

where ΔP is the pressure drop of air; ρ_{air} is the air density and m_{air} is the mass flow rate of air.

The thermal-hydraulic performance of the system measures the improvement in heat transfer as compared to pressure drop due to creating projections over the absorber plate. It is measured in terms of Thermal performance factor (TPF) values. So the following relation has been used for calculating the TPF [38, 39].

$$\mathrm{TPF}=\frac{Nu_{\mathrm{f}}/Nu_{\mathrm{wf}}}{\left(f_{\mathrm{f}}/f_{\mathrm{wf}}\right)^{1/2}} \tag{32}$$

where Nu_{f} and Nu_{wf} are the Nusselt numbers on the fined surface and without the finned surface. The f_{f} and f_{wf} are the friction factors on the finned surface and without the finned surface.

6. Energy Balance for SAH

Now apply the energy balance for the control volume as shown in Fig. 7, where the blue color shows the energy interaction in various forms by fins and cover plate to the AP; the grey color shows the exergy supply to the system and the green color shows the heat supply and losses due to the atmosphere.

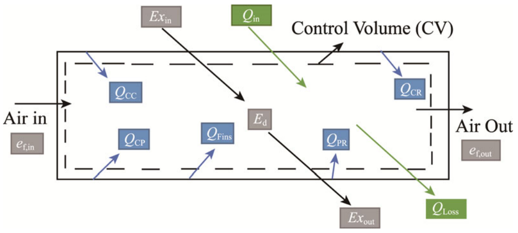

Fig. 7 Energy and exergy interaction with SAH

$$\frac{\mathrm{d}U_{\mathrm{cv}}}{\mathrm{d}t}=Q_{\mathrm{in}}-Q_{\mathrm{loss}}+m_{\mathrm{air}}\left(h_{\mathrm{inlet}}-h_{\mathrm{outlet}}\right) \tag{33}$$

For steady state

$$\mathrm{d}U_{\mathrm{cv}}/\mathrm{d}t=0 \tag{34}$$

$$Q_{\mathrm{in}}=Q_{\mathrm{loss}}+m_{\mathrm{air}}C_{P}\left(T_{\mathrm{outlet}}-T_{\mathrm{inlet}}\right) \tag{35}$$

$$S_F A_P \alpha = Q_{\text{loss}} + m_{\text{air}} C_P \left(T_{\text{outlet}} - T_{\text{inlet}}\right) \tag{36}$$

The efficiency of SAH has been represented by the following equation [19].

$$\eta_{\text{SAH}} = \frac{m_{\text{air}} C_P \left(T_{\text{outlet}} - T_{\text{inlet}}\right)}{S_F A_P \alpha} \tag{37}$$

where T_{outlet}, T_{inlet} is the outlet and inlet temperatures of air passed through the solar air heater; α is the absorptivity of the absorber plate; A_P is the area of the absorber plate surface and S_F is the solar intensity.

The net efficiency is represented by following the formula given in Ref. [40].

$$\eta_{\text{net}} = \frac{Q - \left(W_m / g\right)}{I A_C} \tag{38}$$

where W_m is the power consumed in the blower, and g is given by Ref. [40].

$$g = \eta_F \eta_E \left(1 - \varepsilon_t\right) \phi_C \tag{39}$$

where η_F is the fan efficiency; η_E is the efficiency of the electric engine, and ε_t is the Electric transmission loss coefficient. ϕ_C is the efficiency of the thermal electric conversion process.

Q_{loss} is the heat loss by the SAH in the atmosphere. It is represented in the form of an overall heat transfer coefficient [41].

$$Q_{\text{loss}} = U_{\text{loss}} A_P \left(T_P - T_{\text{average}}\right) \tag{40}$$

U_{loss} is the overall loss coefficient determined by the following equation [41].

$$U_{\text{loss}} = U_t + U_b + U_s \tag{41}$$

The top, bottom, and side loss coefficients have been determined by the energy loss from the top, bottom, and sides.

The thermal resistance circuit is shown in Fig. 8. The heat transfers from AP to the top, bottom, and side surface. The heat transfer from the top, bottom, and sides surfaces is determined by the following equations ([41, 35])

$$Q_t = U_t A_P \left(T_P - T_a\right) \tag{42}$$

$$Q_b = U_b A_P \left(T_P - T_a\right) \tag{43}$$

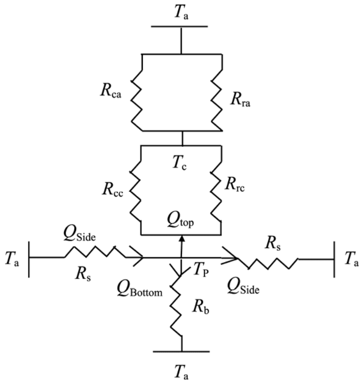

Fig. 8 Thermal resistance circuit for heat transfer for top, bottom, and sides of SAH

$$Q_s = U_s A_P \left(T_P - T_a\right) \tag{44}$$

The overall heat transfer for top surfaces has been determined by

$$\frac{1}{U_t A_P} = \frac{R_{cc} R_{cr}}{R_{cc} + R_{cr}} + \frac{R_{ca} R_{ra}}{R_{ca} + R_{cr}} \tag{45}$$

The R_{cc} and R_{cr} are the convection and radiation resistance between the AP and cover plate [41].

$$R_{cc} = \frac{1}{h_c A_P} \qquad R_{cr} = \frac{\frac{1}{\varepsilon_P} + \frac{1}{\varepsilon_c} - 1}{\sigma\left(T_c + T_P\right)\left(T_P^2 + T_c^2\right)} \tag{46}$$

$$R_{ca} = \frac{1}{h_a A_P} \qquad R_{ra} = \frac{1}{\sigma\left(T_c + T_a\right)\left(T_c^2 + T_a^2\right)} \tag{47}$$

The bottom side thermal resistance is given by the following equation

$$R_b = \frac{t_b}{k_b A_P}, \quad U_b = \frac{k_b}{t_b} \tag{48}$$

The overall side loss coefficient is given by the following equation [42].

$$U_s = \frac{\left(L_{\text{SAH}} + b_{\text{SAH}}\right) H_{\text{SAH}} k_s}{L_{\text{SAH}} b_{\text{SAH}} t_s} \tag{49}$$

where t_b and t_s are the base and side thickness of SAH. L_{SAH}, b_{SAH}, and H_{SAH} are the length, width, and height of SAH. k_s is the thermal conductivity of the side material.

7. Energy Balance for Air by the AP

The heat supplied to the flowing air through the SAH has been supplied by the unfin surface of AP, heat flow through the fins, radiation heat transfer by the absorber plate, and convection and radiation by the glass cover as shown in Fig. 7. The schematic arrangement of heat transfer to the air is shown in Fig. 7.

The following equation represents the heat transfer to the air by the absorber plate and the cover plate [19].

$$\begin{aligned} m_w C_P \left(T_{\text{outlet}} - T_{\text{inlet}}\right) = {} & h A_{\text{unfin}} \left(T_P - T_{\text{air}}\right) + Q_{\text{fins}} \\ & + \varepsilon \sigma A_P \left(T_P^4 - T_{\text{air}}^4\right) \\ & + h A_P \left(T_c - T_{\text{air}}\right) \\ & + \varepsilon_c \sigma A_c \left(T_c^4 - T_{\text{air}}^4\right) \end{aligned} \tag{50}$$

where Q_{fins} is the heat transfer through the fins by Eq. (18). Q_{cc}, Q_{cr} is the heat transfer by convection and radiation by cover plate to the air. Q_{cp} and Q_{rp} are the heat transfer through AP to air by convection and radiation.

8. Exergy Analysis of SAH

Now apply the exergy balance to the solar air heater [43]. The schematic representation of SAH is shown in Fig. 7.

$$\frac{\mathrm{d}Ex_{\mathrm{CV}}}{\mathrm{d}t} = Ex_{\mathrm{in}} - Ex_{\mathrm{out}} + m_{\mathrm{air}}\left(e_{\mathrm{f1}} + e_{\mathrm{f2}}\right) + Ex_{\mathrm{d}} \qquad (51)$$

For steady flow:

$$\mathrm{d}Ex_{\mathrm{CV}}/\mathrm{d}t = 0 \qquad (52)$$

$$Ex_{\mathrm{in}} = Ex_{\mathrm{out}} + m_{\mathrm{air}}\left(e_{\mathrm{f2}} - e_{\mathrm{f1}}\right) + Ex_{\mathrm{d}} \qquad (53)$$

$$Ex_{\mathrm{in}} = m_{\mathrm{air}}\left(e_{\mathrm{f2}} - e_{\mathrm{f1}}\right) + Ex_{\mathrm{out}} + Ex_{\mathrm{d}} \qquad (54)$$

So the exergetic efficiency is given by the following equation [43].

$$\psi = \frac{m_{\mathrm{air}}\left(e_{\mathrm{f2}} - e_{\mathrm{f1}}\right)}{Ex_{\mathrm{in}}} \qquad (55)$$

The e_{f1} and e_{f2} both are the inlet and outlet flow exergy of the air represented in Ref. [43].

$$e_{\mathrm{f1}} = \left(h_1 - h_{\mathrm{o}}\right) - T_{\mathrm{o}}\left(s_1 - s_{\mathrm{o}}\right) \qquad (56)$$

$$e_{\mathrm{f2}} = \left(h_2 - h_{\mathrm{o}}\right) - T_{\mathrm{o}}\left(s_2 - s_{\mathrm{o}}\right) \qquad (57)$$

where h_{o}, T_{o} and s_{o} are the specific enthalpy, atmospheric temperature and specific entropy at atmosphere temperature. The h_1, s_1, h_2 and s_2 are the enthalpy and entropy at inlet and outlet temperature of air.

The $m_{\mathrm{air}}(e_{\mathrm{f2}}–e_{\mathrm{f1}})$ is the gain in exergy of the air due to the heating of air by the AP. The Ex_{out} is the loss in exergy in the atmosphere due to loss of heat and E_{d} is the exergy destruction due to the presence of irreversibility in the SAH. The exergy entering the system is represented by the Ex_{in}.

The exergy loss in the atmosphere is represented by the equation [44]:

$$Ex_{\mathrm{out}} = \left(1 - \frac{T_{\mathrm{a}}}{T_{\mathrm{P}}}\right) Q_{\mathrm{out}} \qquad (58)$$

The exergy entering the SAH depends on the sun temperature, heat flux, and atmospheric temperature. It is represented by the following equation [44].

$$Ex_{\mathrm{in}} = A_{\mathrm{P}} S_{\mathrm{F}} \left[1 - \frac{4}{3}\left(\frac{T_{\mathrm{a}}}{T_{\mathrm{sun}}}\right) + \frac{1}{3}\left(\frac{T_{\mathrm{a}}}{T_{\mathrm{sun}}}\right)^4\right] \qquad (59)$$

Exergy loss to the atmosphere

$$Ex_{\mathrm{out}} = Q_{\mathrm{out}}\left[1 - \frac{T_{\mathrm{a}}}{T_{\mathrm{P}}}\right] \qquad (60)$$

The useful exergy gain is represented by the following equation [43].

$$m_{\mathrm{air}}\left(e_{\mathrm{f2}} - e_{\mathrm{f1}}\right) = m_{\mathrm{air}}\left\{C_P\left(T_{\mathrm{outlet}} - T_{\mathrm{inlet}}\right) - T_{\mathrm{o}}\left[C_P \ln\left(\frac{T_{\mathrm{outlet}}}{T_{\mathrm{inlet}}}\right) - R\ln\left(\frac{p_2}{p_1}\right)\right]\right\} \qquad (61)$$

The exergy destruction Ex_{d} is determined by Eq. (51).

9. Experimental Set-Up

Fig. 9 shows the simple solar air heater with triangular fins (SSAHF). The triangular fins are used for increasing the HT between the AP and air. A total of 94 triangular fins of height 2.54 cm and a base width of 5 cm were used on the absorber plate in a regular pattern. The one fin base center to the other fin base center distance was maintained to be 10.33 cm. Fig. 10 shows the schematic representation of the experimental setup of SSAHF with a thermocouple mounted on the top, middle, and bottom parts of the AP. Thermocouples 3, 4, and 5 were used on the tampered glass cover, and 1 and 2 were used for measuring the temperatures of the inlet air and outlet air of the SAH. The anemometer is used for measuring the inlet air velocity as shown in Fig. 11, which is further used for measuring the MFR of air. The U-tube mercury-filled glass tube is used for measuring the pressure drop along the length of SAH.

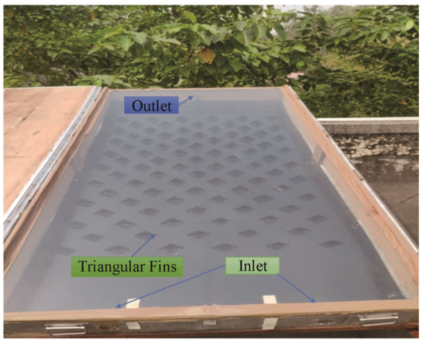

Fig. 9 Triangular-type finned SAH

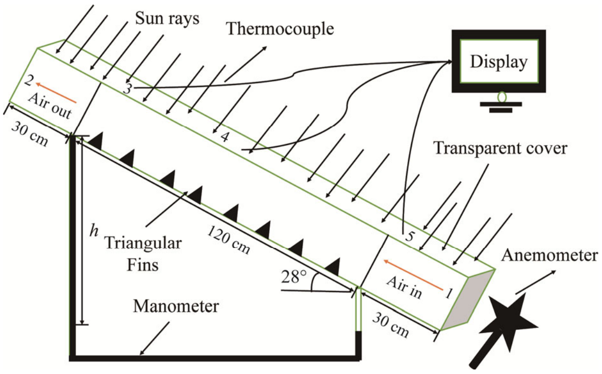

Fig. 10 Schematic representation of the experimental setup

The SAH has been inclined at 28° from horizontal (Latitude of Bareilly, Uttar Pradesh, India). It is already assumed that the temperature in the direction of the width of AP remains constant. So the average temperature of AP (T_{P}) has been determined by the average temperature of the thermocouple placed at the top, bottom, and middle part of SAH. The average temperature of the AP helps to determine the heat transfer coefficient and total heat transfer by the SAH. The further efficiency of SAH has been determined by Eq. (37). The exergetic efficiency of SAH has been determined by Eq. (55) after measuring the outlet and inlet air temperature. Fig. 11

shows the pictorial view of various instruments like an anemometer, temperature thermocouple display device, pyranometer, and temperature measurement by contacting knobe.

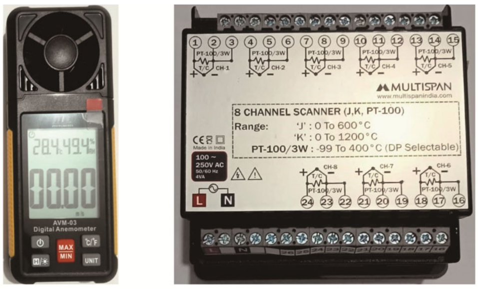

(a) Anemometer (b) 8 Channel thermocouple connector

(c) Pyranometer (d) Multi thermometer

Fig. 11 Instruments used for the experimental work

10. Uncertainty Analysis

The experimental data in SAH have been collected for determining the performance of SAH. The inlet air velocity has been determined by the anemometer and further inlet air velocity is used for determining the mass flow rate of air. The inlet and outlet temperatures are measured by the thermocouples which are further used for determining the heat gain by the air. The absorber plate average temperature is used for determining the heat loss and loss in exergy from the SAH. These input variables measured by the measuring device always have some uncertainty which further increases the inaccuracy of the results of the response parameters. The inaccuracy of the response or output parameters depends on the model equations. So following are the model equation used for determining the accuracy of the output parameters.

The efficiency of SAH is the function of $\eta_{\mathrm{I}}=f(s, T_{\mathrm{out}}, T_{\mathrm{in}}, m)$, so the uncertainty equation of solar air heater efficiency.

$$y\eta_{\mathrm{I}} = \left[\left(\frac{\delta\eta_{\mathrm{I}}}{\delta m}\right)^2 y_m^2 + \left(\frac{\delta\eta_{\mathrm{I}}}{\delta T_{\mathrm{out}}}\right)^2 y_{T_{\mathrm{out}}}^2 + \left(\frac{\delta\eta_{\mathrm{I}}}{\delta T_{\mathrm{in}}}\right)^2 y_{T_{\mathrm{in}}}^2 + \left(\frac{\delta\eta_{\mathrm{I}}}{\delta s}\right)^2 y_s^2\right]^{1/2} \tag{62}$$

The solar air heater's exergy efficiency $\eta_{\mathrm{II}}=f(s, m, T_{\mathrm{out}}, T_{\mathrm{in}}, P_{\mathrm{out}}, P_{\mathrm{in}})$, so the uncertainty in exergy efficiency is represented by the following equation. So the uncertainty in the exergy efficiency is

$$y\eta_{\mathrm{II}} = \left[\left(\frac{\delta\eta_{\mathrm{II}}}{\delta m}\right)^2 y_m^2 + \left(\frac{\delta\eta_{\mathrm{II}}}{\delta T_{\mathrm{out}}}\right)^2 y_{T_{\mathrm{out}}}^2 + \left(\frac{\delta\eta_{\mathrm{II}}}{\delta T_{\mathrm{in}}}\right)^2 y_{T_{\mathrm{in}}}^2 + \left(\frac{\delta\eta_{\mathrm{II}}}{\delta P_{\mathrm{in}}}\right)^2 y_{P_{\mathrm{in}}}^2 + \left(\frac{\delta\eta_{\mathrm{II}}}{\delta P_{\mathrm{out}}}\right)^2 y_{P_{\mathrm{out}}}^2 + \left(\frac{\delta\eta_{\mathrm{II}}}{\delta s}\right)^2 y_s^2\right]^{1/2} \tag{63}$$

The exergy destruction is also the function of the MFR, solar intensity, an inlet temperature of atmospheric air, the outlet temperature of atmospheric air, inlet air pressure, and outlet air pressure. So uncertainty equation in the exergy destruction is represented by the following equation.

$$y_{Ex_{\mathrm{d}}} = \left[\left(\frac{\delta Ex_{\mathrm{d}}}{\delta m}\right)^2 y_m^2 + \left(\frac{\delta Ex_{\mathrm{d}}}{\delta T_{\mathrm{out}}}\right)^2 y_{T_{\mathrm{out}}}^2 + \left(\frac{\delta Ex_{\mathrm{d}}}{\delta T_{\mathrm{in}}}\right)^2 y_{T_{\mathrm{in}}}^2 + \left(\frac{\delta Ex_{\mathrm{d}}}{\delta P_{\mathrm{in}}}\right)^2 y_{P_{\mathrm{in}}}^2 + \left(\frac{\delta Ex_{\mathrm{d}}}{\delta P_{\mathrm{out}}}\right)^2 y_{P_{\mathrm{out}}}^2 + \left(\frac{\delta Ex_{\mathrm{d}}}{\delta s}\right)^2 y_s^2\right]^{1/2} \tag{64}$$

The inlet and outlet air temperatures have been measured by the thermocouple with ±4% accuracy; the inlet velocity of air has been measured with the help of an anemometer with an accuracy of ±3%, and the MFR is calculated by the air entering velocity. The PD has been calculated by U tube inclined manometer of accuracy ±5%, and the solar intensity is measured by the pyranometer with an accuracy of 5%. So the total uncertainty of input and output parameters is given in Table 3.

Table 3 Uncertainty in input parameters

No.	Parameter	Instruments	Uncertainty
1	Temperature measurement	Thermocouples	4.25%
2	Pressure measurement	Manometer	4.10%
3	Velocity measurement	Anemometer	4%
4	Solar Intensity	Pyranometer	4.89%
5	Solar air heater efficiency	–	3.56%
6	Exergy efficiency	–	4.12%
7	Exergy destruction	–	4.95%

11. Optimization of SAH

For optimizing the performance of the SAH Response Surface Methodology (RSM) technique has been used in MINITAB 17 software. The RSM is the optimizing tool used for determining the optimal setting of input variables on which output responses will be the maximum or minimum. It was the first time used in 1951 by George E.P. Box and K.B. Wilson. This technique used the second-order polynomial of response parameters in terms of input variables since the second-order polynomial is easily fitted even with little knowledge about the process. In this research initial response surface design has been created in which three major influencing input variables have been selected for defining the problem namely solar intensity, Reynolds Number, and fin base-to-height ratio. The range of the input variables and their code in RSM is given in Table 4.

In Table 4, –1, 0, and +1 represent the minimum, average, and maximum values of the input variables respectively. The Box Behenken Design (BBD) has been used for defining the input variables design matric as compared to Central Composite Design (CCD) since BBD requires a small number of runs as compared to the CCD design approach. Now L15 array matrix has been created. Table 5 shows the response parameter values as compared to the L15 array input parameters setting.

The data presented in Table 4 is converted in the second order polynomial by Analysis of Variance (ANOVA) which responses like outlet temperature, friction factor, Nusselt number, efficiency, exergy efficiency, and TPF are represented in terms of input variables. The following regression equation has been generated by the ANOVA analysis.

$$\begin{aligned} T = {} & -31.7 + 0.955 S_{\mathrm{F}} - 0.0123 Re + 70.9 F_{\mathrm{b/h}} \\ & - 0.000\,035 S_{\mathrm{F}}^{2} + 0.000\,001 Re^{2} - 71.7 F_{\mathrm{b/h}} \\ & - 0.000\,005 S_{\mathrm{F}} Re - 0.003\,3 S_{\mathrm{F}} F_{\mathrm{b/h}} \\ & + 0.003\,82 Re F_{\mathrm{b/h}} \end{aligned} \tag{65}$$

$$\begin{aligned} f = {} & -0.456 + 0.002\,841 S_{\mathrm{F}} - 0.000\,245 Re + 1.159 F_{\mathrm{b/h}} \\ & - 0.000\,001 S_{\mathrm{F}}^{2} - 0.553 F_{\mathrm{b/h}}^{2} \\ & - 0.000\,107 S_{\mathrm{F}} F_{\mathrm{b/h}} + 0.000\,065 Re F_{\mathrm{b/h}} \end{aligned} \tag{66}$$

$$\begin{aligned} Nu = {} & -0.456 + 0.002\,841 S_{\mathrm{F}} - 0.000\,245 Re \\ & + 1.159 F_{\mathrm{b/h}} - 0.000\,001 S_{\mathrm{F}}^{2} - 0.553 F_{\mathrm{b/h}}^{2} \\ & - 0.000\,107 S_{\mathrm{F}} F_{\mathrm{b/h}} + 0.000\,065 Re F_{\mathrm{b/h}} \end{aligned} \tag{67}$$

$$\begin{aligned} \eta = {} & -55.4 + 0.252\,1 S_{\mathrm{F}} - 0.015\,4 Re + 66.3 F_{\mathrm{b/h}} \\ & - 0.000\,114 S_{\mathrm{F}}^{2} + 0.000\,001 Re^{2} \\ & - 68.5 F_{\mathrm{b/h}}^{2} - 0.000\,001 S_{\mathrm{F}} Re \\ & - 0.001\,9 S_{\mathrm{F}} F_{\mathrm{b/h}} + 0.003\,75 Re F_{\mathrm{b/h}} \end{aligned} \tag{68}$$

Table 4 Input values range and code values

		Code		
Input parameters	symbols	–1 (Minimum)	0 (Average)	1 (Maximum)
Solar intensity/W·m^{-2}	S_{F}	600 W/m^2	800 W/m^2	1000 W/m^2
Reynolds number	Re	4000	5000	6000
Fin base-to-height ratio	$F_{\mathrm{b/h}}$	0.4	0.6	0.8

Table 5 L15 array of input and response variables

No.	Solar Intensity /W·m^{-2}	Reynolds number Re	Fin base-to-height ratio $F_{\mathrm{b/h}}$	Outlet Temperature /°C	Friction factor	Nusselt number	Efficiency /%	Exergy efficiency /%	TPF
1	800	5000	0.6	71.410 0	0.221 949	76	28.798 9	7.10	1.530
2	800	5000	0.6	71.400 0	0.220 000	135.587 5	45.598 3	7.08	1.529
3	600	5000	0.8	44.738 2	0.113 992	136.138 1	42.598 4	3.65	1.510
4	600	4000	0.6	50.011 8	0.271 362	152.795 9	53.9	4.80	1.520
5	600	6000	0.6	44.508 9	0.077 890	60	47.998 2	3.60	1.570
6	800	6000	0.4	62.240 6	0.100 241	144.687 9	37.6	5.60	1.420
7	800	6000	0.8	65.297 8	0.127 542	130	56.35	6.10	1.520
8	800	4000	0.8	74.469 4	0.392 099	136.138 1	41.398 5	7.60	1.510
9	1000	6000	0.6	89.144 0	0.088 404	49	22.199 2	8.00	1.300
10	1000	5000	0.8	88.379 7	0.220 529	137.035 3	54.36	7.90	1.501
11	600	5000	0.4	44.967 5	0.092 152	105	21.899 2	3.70	1.400
12	800	5000	0.6	70.189 4	0.237 838	119	68.9	6.90	1.570
13	800	4000	0.4	74.469 4	0.312 500	136.138 1	41.398 5	7.60	1.400
14	1000	4000	0.6	99.000 0	0.407 784	88	55.735 2	10.40	1.515
15	1000	5000	0.4	89.144 0	0.215 789	120.044 5	47.998 2	8.00	1.490

$$\begin{aligned}\eta_{\mathrm{ex}} &= -10.16 + 0.044\,06 S_{\mathrm{F}} - 0.015\,4 Re + 66.3 F_{\mathrm{b/h}} \\ &\quad - 0.000\,114 {S_{\mathrm{F}}}^2 + 0.000\,001 Re^2 \\ &\quad - 68.5 {F_{\mathrm{b/h}}}^2 - 0.000\,001 S_{\mathrm{F}} Re \\ &\quad - 0.001\,9 S_{\mathrm{F}} F_{\mathrm{b/h}} + 0.003\,75 Re F_{\mathrm{b/h}}\end{aligned} \tag{69}$$

$$\begin{aligned}\mathrm{TPF} &= -1.85 + 0.002\,99 S_{\mathrm{F}} + 0.000\,653 Re \\ &\quad + 1.99 F_{\mathrm{b/h}} - 0.000\,001 {S_{\mathrm{F}}}^2 - 1.019 {F_{\mathrm{b/h}}}^2 \\ &\quad - 0.000\,619 S_{\mathrm{F}} F_{\mathrm{b/h}} - 0.000\,013 Re F_{\mathrm{b/h}}\end{aligned} \tag{70}$$

Eqs. (65)–(70) represent the responses in terms of input variables in which T, f, Nu, η, η_{ex}, and TPF are the outlet temperature, friction factor, Nusselt number, efficiency, exergy efficiency and thermal performance factor. The S_{F}, Re, and $F_{\mathrm{b/h}}$ are represented as solar intensity, Reynolds number, and the fin base-to-height ratio.

The accuracy of the responses was tested by the S, $R^{2,}$ and R^2(adj) values generated after the ANOVA analysis. The S, R^2, R^2(adj) is known as the standard error, square error, and square of adjusted error. The following equations are used for calculating the S, R^2, and R^2(adj) values.

$$S = \frac{\sigma}{N^{1/2}} \tag{71}$$

$$R^2 = 1 - \frac{S_{\mathrm{res}}^2}{S_{\mathrm{total}}^2} \tag{72}$$

$$R^2 = 1 - \frac{\sum_{i=1}^{15} \left(x_i - x_i'\right)^2}{\sum_{i=1}^{15} \left(x_i - \bar{x}_i\right)^2} \tag{73}$$

$$R^2\left(\mathrm{adj}\right) = 1 - \frac{\left(1 - R^2\right)\left(N - 1\right)}{N - M - 1} \tag{74}$$

where x represents the responses like T, f, Nu, η, η_{ex}, and TPF. The i represents the total number of experimental observations from 1, 2, 3…….15. N is the total number of runs and M represents the independent variables or input variables. The R^2 value between 70% to 100% gives good results. Table 6 represents the S, $R^{2,}$ and R^2(adj) values of the responses.

Table 6 Errors in responses

No.	Responses	S	R^2	R^2(adj)
1	Outlet Temperature (T)	1.54	99.73%	99.24%
2	Friction factor (f)	1.65	98.75%	96.49%
3	Nusselt number (Nu)	1.4	99.24%	98.16%
4	Efficeincy (η)	1.26	99.52%	98.65%
5	Exergy (η_{ex})	1.7	99.36%	98.20%
6	TPF	1.62	72.24%	70.24%

Table 5 shows the good accuracy of the results since all values of R^2 are greater than 70% even the model is best fitted with an accuracy of more than 95%.

12. Result and Discussion

In this section, the surface plot and contour plot of Nusselt Number, friction factor, outlet temperature, thermal efficiency, exergy efficiency, and thermal-hydraulic performance with respect to input parameters Reynolds number, solar intensity, and fin base to height ratio have been drawn in MINITAB 17 software. The inlet-outlet temperature, average absorber plate temperature, inlet velocity of air, and pressure drop were determined experimentally. The Response parameters like Nusselt number, friction factor, thermal efficiency, exergy, and THP have been determined by Eqs. (1) to (61). Furthermore, with the help of experimental findings and modeled equations, the data has been optimized and the results obtained are explained in the below sections.

12.1 Variation of outlet temperature with input variables

Fig. 12 shows the surface and contour plot of the outlet temperature of the air from the solar air heater. Fig. 12(a) shows that if solar intensity increases, then outlet temperature increases since higher solar intensity increases the heat supply to the SAH. Fig. 12(a) also depicted that an increase in Reynolds number reduces the outlet temperature of air since the increase in Reynolds number increases the mass flow rate of air [14, 31]. Fig. 12(b) represents the contour plot of the outlet temperature which shows that outlet temperature is the maximum at high solar intensity and low Reynolds Number [45].

Fig. 12(c) depicted that the initial increase in the fin base to height ratio from 0.4 to 0.6 increases the outlet temperature but with a further increase in the fin base to height ratio the outlet temperature is reduced. Fig. 12(d) contour plot shows that the maximum outlet temperature is obtained at 1000 W/m^2 and near the fin base to height ratio of 0.6.

Fig. 12(e) and 12(f) also show that outlet temperature is the maximum at the lower Reynolds number and fins base-to-height ratio of 0.6 since an initial increase in the base of the fins increases the turbulence but the further increase in the base of fin promotes the blocked flow which reduces the turbulence in the SAH [46].

12.2 Variation of friction factor with input variables

Fig. 13 shows the variation of the friction factor with the input variables. Fig. 13(a) shows that an increase in

Reynolds number reduces the friction factor as per Eqs. (28) and (29) [47] but initially increase in solar intensity increase the friction factor but after attaining the maximum friction factor further increase in solar intensity reduces the friction factor [48]. Initially when solar intensity increases, the temperature of the air start increasing due to that density reduction takes place which reduces the Reynolds number and results in friction

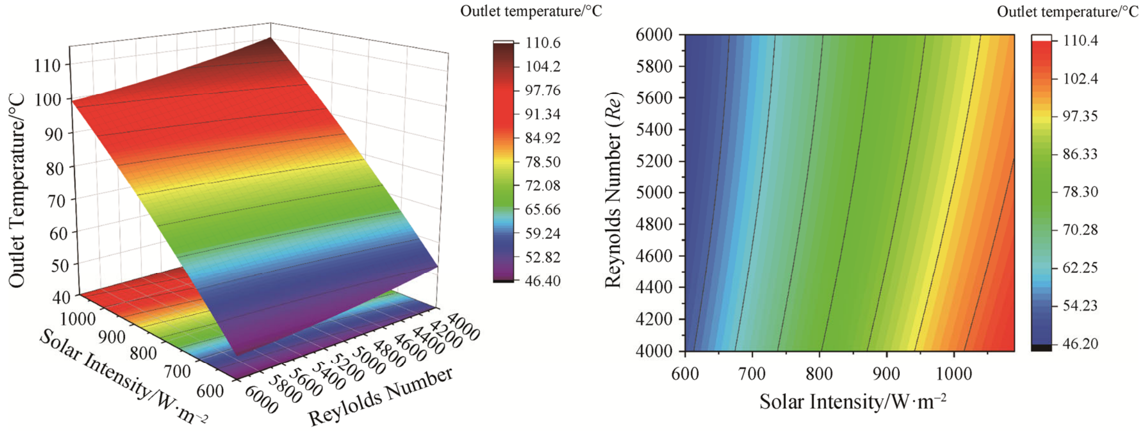

(a) Outlet temperature variation with Reynolds Number and solar intensity

(b) Contour plot of outlet temperature with Solar Intensity and Reynolds Number

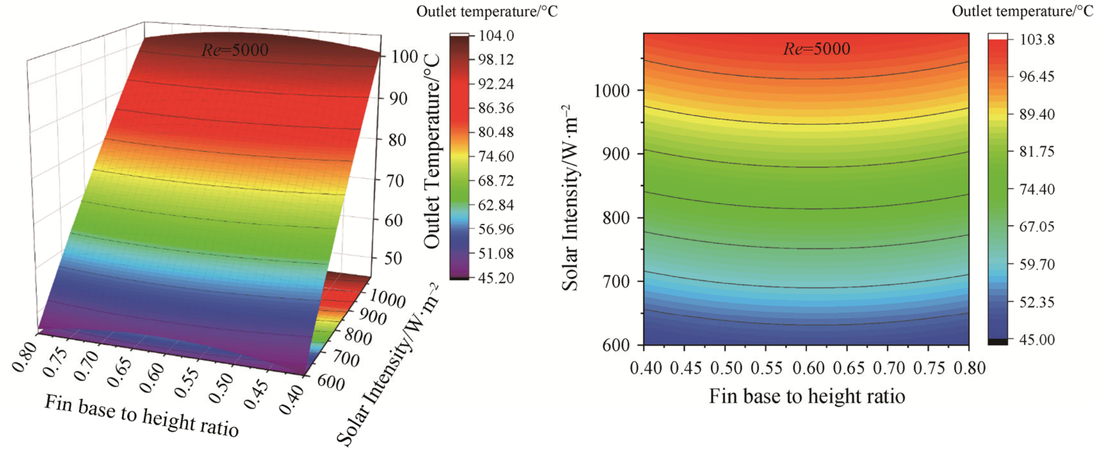

(c) Outlet temperature variation with fin base to height ratio and solar intensity

(d) Contour plot of outlet temperature with Solar Intensity and fin base-to-height ratio

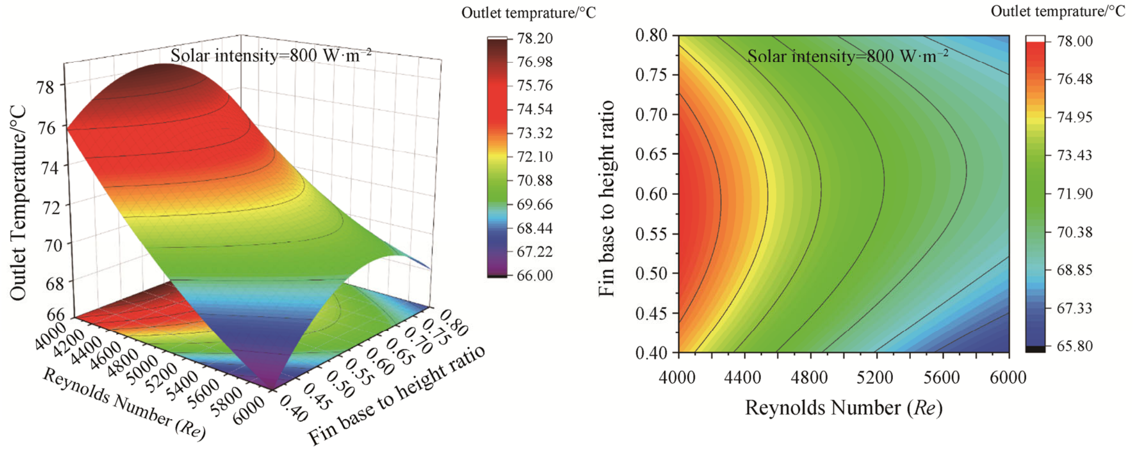

(e) Outlet temperature variation with fin base to height ratio and Reynolds Number

(f) Contour plot of outlet temperature with Reynolds Number and fin base-to-height ratio

Fig. 12 Variation of outlet temperature with input variables factor increase. But, when solar intensity is more than 800 W/m^2, the temperature of the air is quite high since the viscosity reduction is higher than the density which enhances the Reynolds number and results in a reduction in friction factor [49]. Fig. 13(b) shows that a lower friction factor was obtained at a lower solar intensity and higher values of Reynolds number.

Fig. 13(c) and 13(d) show that if the fin base height ratio increases, then the friction factor increases but after attaining the optimum values it starts to reduce due to the increase in turbulence in the flow path of air [12]. The friction factor shows the same trends as Reynolds number and the fins base-to-height ratio as seen in Figs. 13(e) and 13(f).

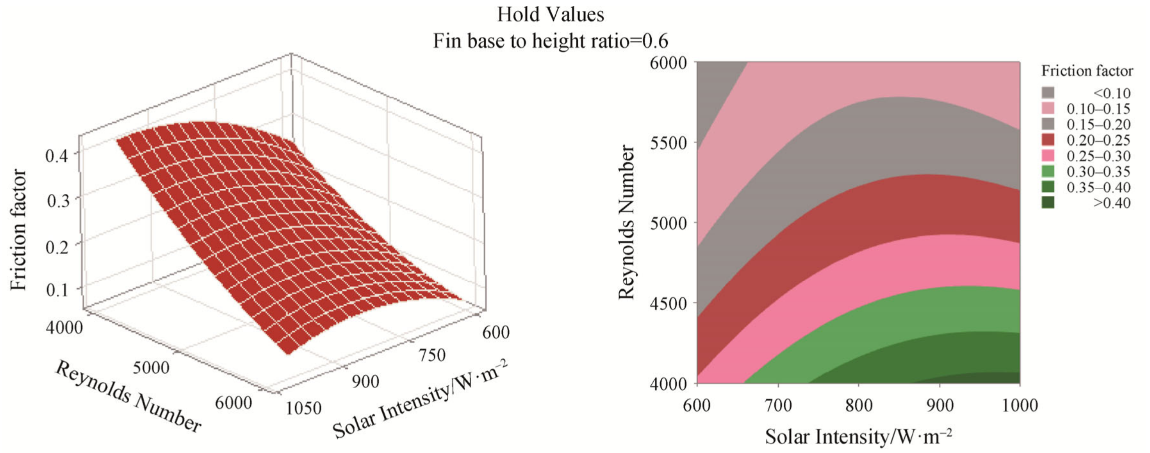

(a) Friction Factor variation with Reynolds Number and Solar Intensity

(b) Contour plot of Friction Factor with Solar Intensity and Reynolds Number

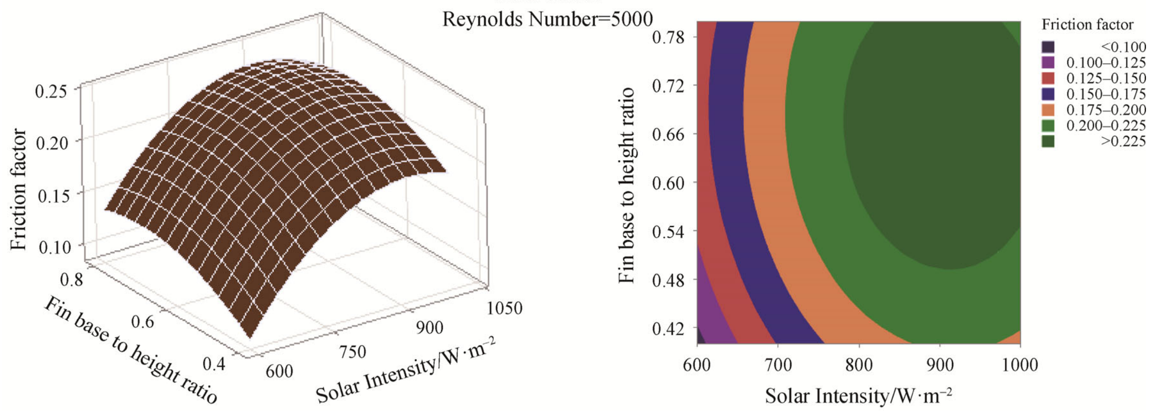

(c) Friction Factor variation with fin base to height ratio and Solar Intensity

(d) Contour plot of Friction Factor with Solar Intensity and fin base-to-height ratio

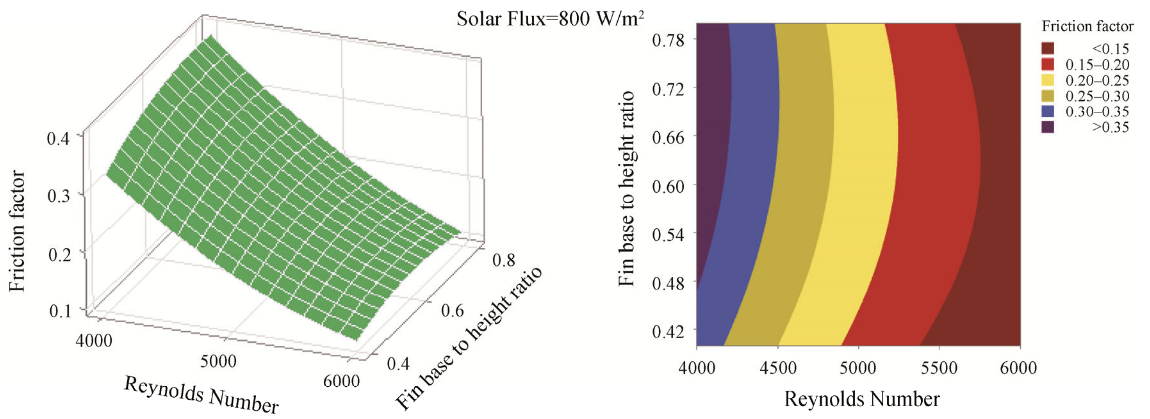

(e) Friction Factor variation with fin base to height ratio and Reynolds Number

(f) Contour plot of Friction Factor with Reynolds Number and fin base-to-height ratio

Fig. 13 Variations of friction factor with input variables

12.3 Nusselt number variation with input variables

Fig. 14 depicts the Nusselt number variation with the solar intensity, Reynolds number, and the fin base-to-height ratio. Fig. 14(a) and 14(b) show that if solar intensity and Reynolds number increase, then the Nusselt number increases [25]. Eq. (25) shows the dependence of the Nusselt number on the Reynolds number. The equation shows that if Reynolds number

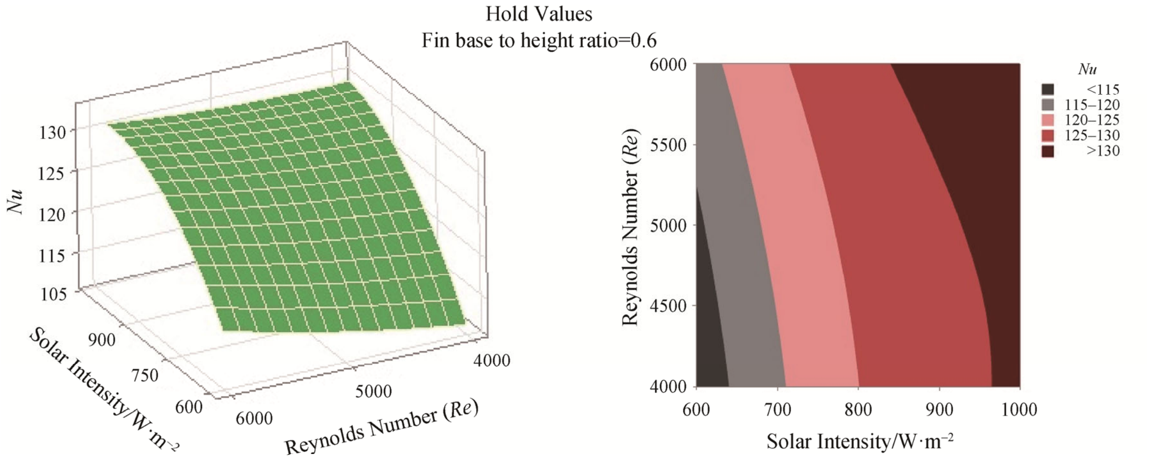

(a) Nusselt Number variation with Reynolds Number and solar intensity

(b) Contour plot of Nusselt Number with Solar Intensity and Reynolds Number

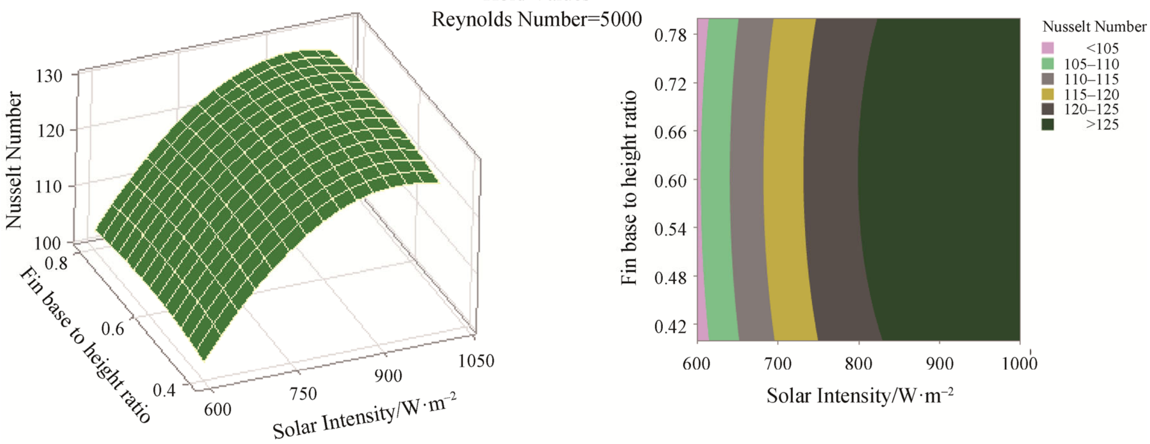

(c) Nusselt Number variation with fin base to height ratio and solar intensity

(d) Contour plot of Nusselt Number with Solar Intensity and fin base-to-height ratio

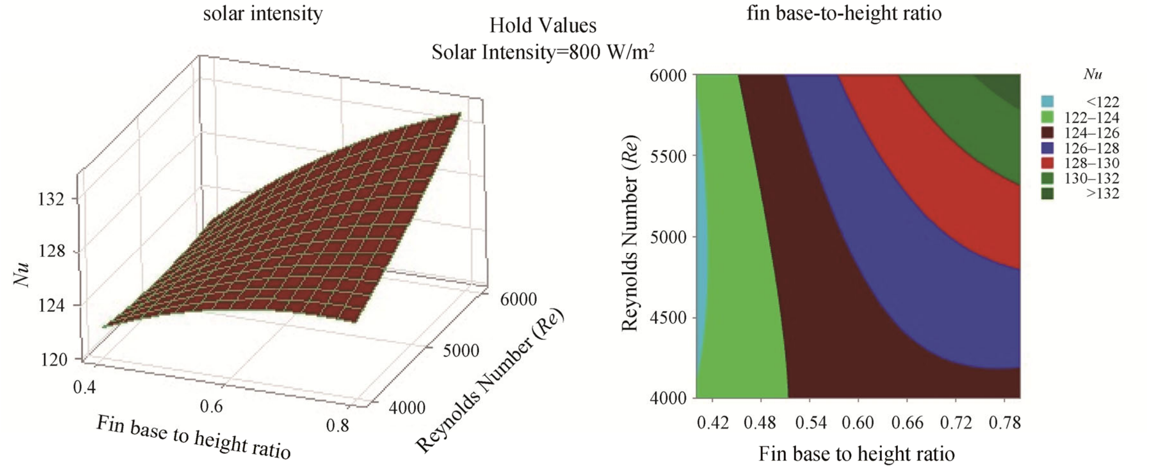

(e) Nusselt Number variation with fin base to height ratio and Reynolds Number

(f) Contour plot of Nusselt Number with Reynolds Number and fin base-to-height ratio

Fig. 14 Nusselt number variation with the input variables increases, then the Nusselt number increases since the increase in Reynolds number enhances the turbulence of air inside SAH. Fig. 14(c)–(f) also prove the validity of the results and also show that the fin base height ratio does not much affect Nusselt number, but at optimum values of 0.6, Nusselt number increases, while the further increase in the fin base to height ratio reduces Nusselt number [50].

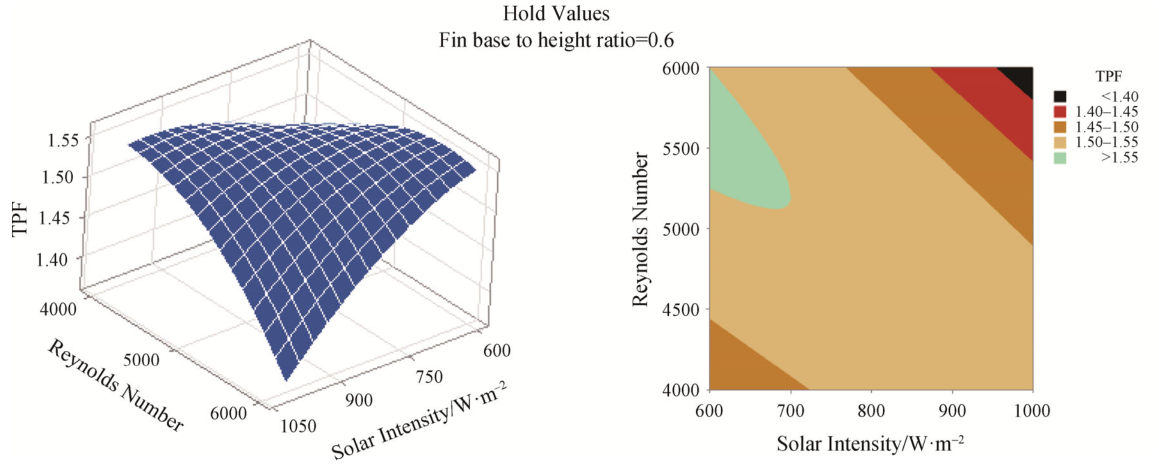

(a) TPF variation with Reynolds Number and solar intensity

(b) Contour plot of TPF with Solar Intensity and Reynolds Number

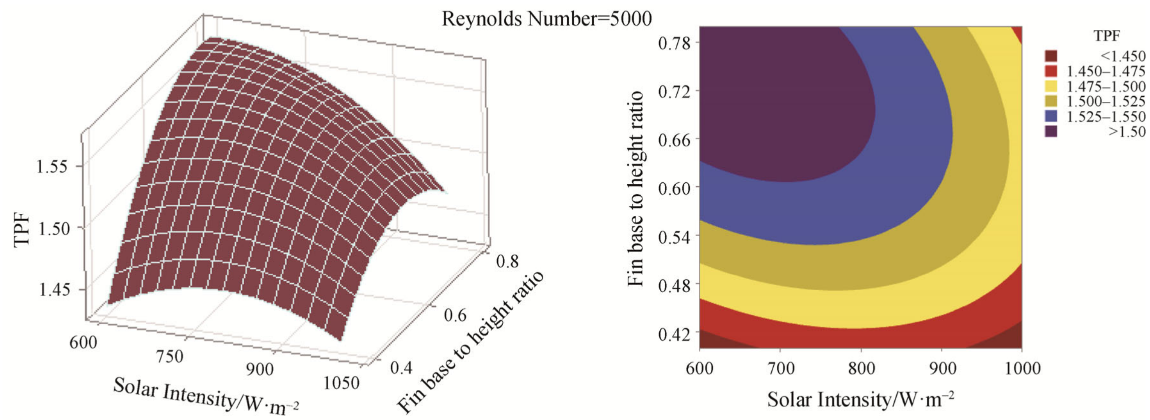

(c) TPF variation with fin base to height ratio and solar intensity

(d) Contour plot of TPF with Solar Intensity and fin base-to-height ratio

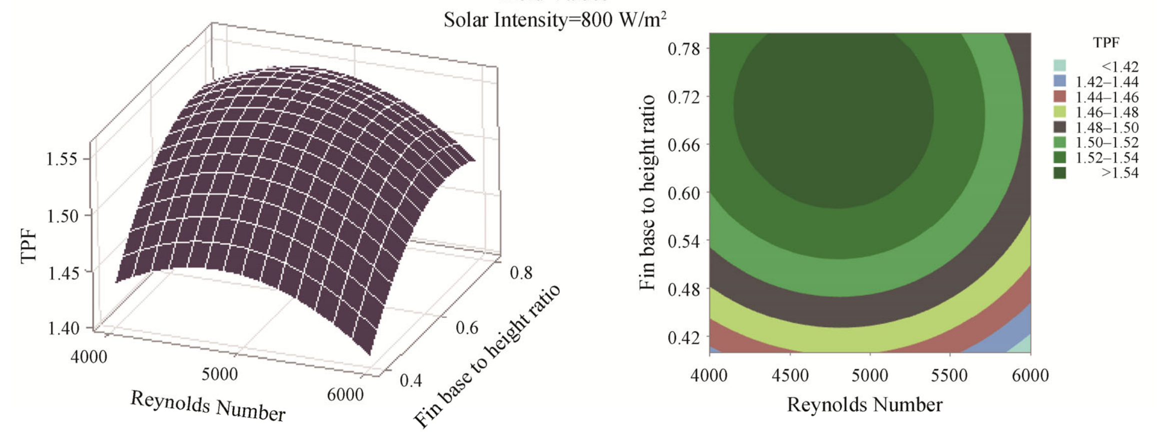

(e) TPF variation with fin base to height ratio and Reynolds Number

(f) Contour plot of TPF with Reynolds Number and fin base-to-height ratio

Fig. 15 TPF variation with the input variables

12.4 TPF variation with the input variables

Thermal Performance Factor (TPF) is a very important parameter for measuring the relative measurement of heat transfer as compared to friction. The higher values of TPF justify the fin production on the surface of the absorber plate. Fig. 15 shows that the increases in solar intensity, Reynolds number, and the fin base-to-height ratio initially increase the TPF, and after attaining the optimum values, the TPF values start to reduce [14]. The optimum value of TPF is 1.52 which has a good achievement for promoting heat transfer in SAH [38].

12.5 Efficiency variation with Input variables

Fig. 16(a) depicted that if the solar intensity increases, the efficiency of the solar air heater increases since the increase in solar flux heat transfer rate is enhanced. The increase in Reynolds number enhances the system efficiency due to an increase in mass flow rate. Fig. 16(b) shows a contour plot that also shows that the SAH has efficiency greater than 55% at a higher solar intensity at a low Reynolds number [51]. Fig. 16(c) shows that the increase in the fin base to height ratio increases the efficiency of SAH, but after attaining the optimum value, the increase in base to the height of the fin reduces the fin efficiency. Fig. 16(d) contour plots that the higher solar intensity and the medium base to height region corresponds to the maximum efficiency. Fig. 16(e) and (f) show the same trends of efficiency with Reynolds number, solar intensity, and the fin base to height ratio as explained above [16].

12.6 Exergy efficiency variation with input variables

Fig. 17(a) shows that if solar intensity increases the exergy efficiency of SAH increases since the solar intensity enhances the gain in exergy but on the other hand, the enhancement in Reynolds number reduces the exergy efficiency since the mass flow and blower power increase with Reynolds number [52]. Fig. 17(b) shows the contour plot of the exergy. It is seen from Fig. 17(b) that higher solar intensity at a low Reynolds number gives the maximum exergy. Fig. 17(c) surface plot shows that the fin base to height ratio increase increases the exergy, but after attaining the optimum value, it starts to reduce. Fig. 17(d) contour plot at mid shows the maximum exergy which shows the higher solar intensity and medium base-to-height ratio of the fin. Fig. 17(e) and (f) also show the same variation of exergy with Reynolds number and the fin base-to-height ratio, as explained in Fig. 17(c) and (d).

12.7 Optimization plot of responses with input variables

Fig. 18 shows the optimum values of the input variables at which responses are maximum and minimum. The optimum values of solar intensity, Reynolds number, and the fin base-to-height ratio are 1000 W/m^2, 4969.6970, and 0.6061. These optimum settings of input variables responses like outlet temperature, friction factor, Nusselt number, TPF, efficiency, and exergy efficiency are 92.5307°C, 0.2350, 127.7614, 1.4947, 50.83%, and 8.7624%. The overall desirability of the results is 0.7749 which shows the accuracy of the results.

12.8 Validation of RSM predicted results with experimental results

For validating the optimum setting of input variables and responses, the experimental setup of the solar air heater run at the optimum setting of input variables like solar intensity of 1000 W/m^2, Reynolds number of 4969.6970, and the fin base-to-height ratio of 0.6061. Table 7 shows the experimental results and percentage with respect to predicted results of RSM and it is found that results are satisfactorily validated with a maximum percentage error of 5%.

12.9 Variation of Nusselt number, friction factor, thermal efficiency, and outlet temperature with Reynolds number

12.9.1 Nusselt number variation with Reynolds number

Fig. 19 displays the variation of Nusselt number with Reynolds number. It shows as Reynolds number increases, Nusselt number also increases, and the same trends are also seen in Ref. [53]. The increase in Reynolds number enhances the turbulence of air inside the SAH which promotes the heat transfer and Nusselt number.

12.9.2 Friction factor and thermal efficiency variation with Reynolds number

Fig. 20 depicts the variations of thermal efficiency and friction factor with Reynolds number. In Fig. 20, thermal efficiency variation shows that if the Reynolds number increases, the thermal efficiency increases since the increase in Reynolds number increases the mass flow rate and the heat transfer. The variation of friction factor with the Reynolds number is just the reverse of the efficiency. The increase in Reynolds number reduced the friction factor [30].

12.9.3 Outlet temperature variation with Reynolds number

Fig. 21 shows that the increased Reynolds number reduced the outlet temperature since the increase in Reynolds number increases the mass flow rate of air. The increase in mass flow rate enhances the useful heat gain which promotes the thermal efficiency of solar air heaters but reduces the outlet temperature [54].

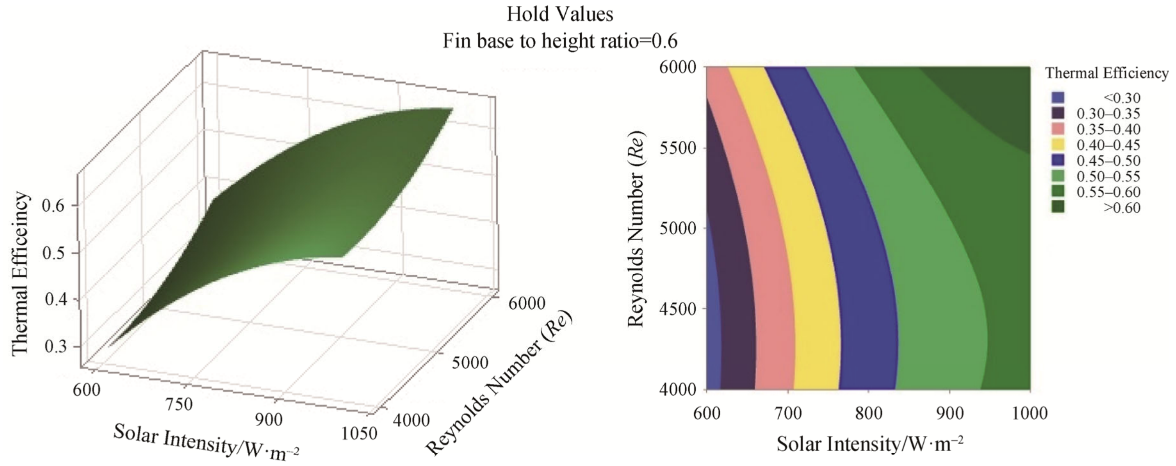

(a) Efficiency variation with Reynolds Number and solar intensity

(b) Contour plot of efficiency with Solar Intensity and Reynolds Number

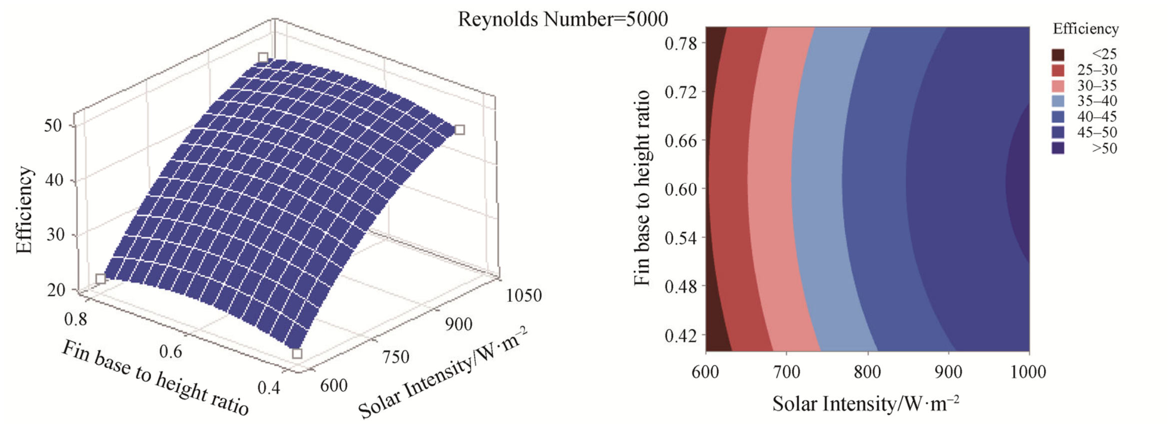

(c) Efficiency variation with fin base-to-height ratio and solar intensity

(d) Contour plot of efficiency with Solar Intensity and fin base-to-height ratio

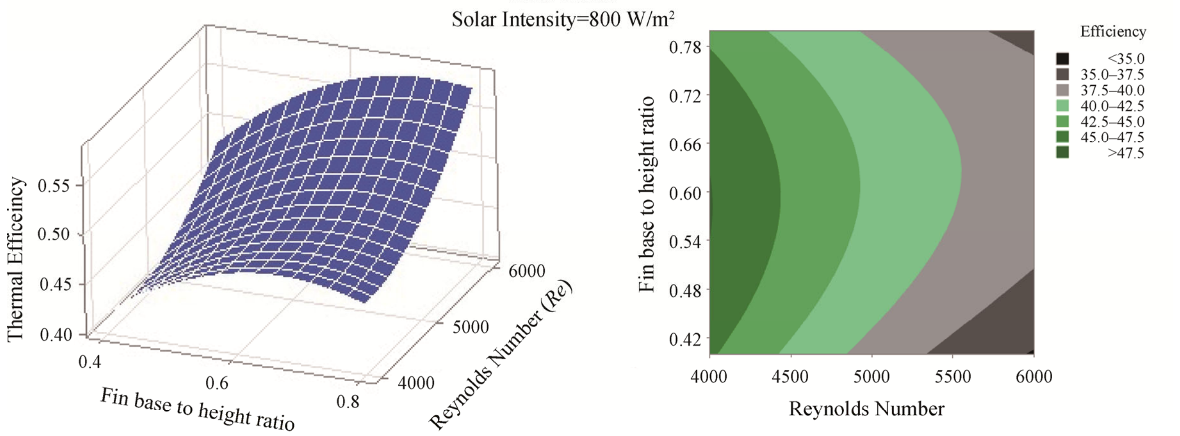

(e) Efficeicy variation with fin base to height ratio and Reynolds Number

(f) Contour plot of efficiency with Reynolds Number and fin base-to-height ratio

Fig. 16 Efficiency variation with the input variables

12.9.4 Validation of thermal-hydraulic performance with the previously published results of Mukesh Kumar Sahu et al. [53]

Fig. 22 clearly shows that the triangular shape Fins give a higher THP than the arc-shaped apex upstream (Mukesh Kumar Sahu et al. [53]). The maximum values of THP in the present study and arc-shaped apex have been noted to be 1.79 and 1.59 at Reynolds number of 6000. The higher values of the THP show the benefits of the roughness as compared to the smooth surface.

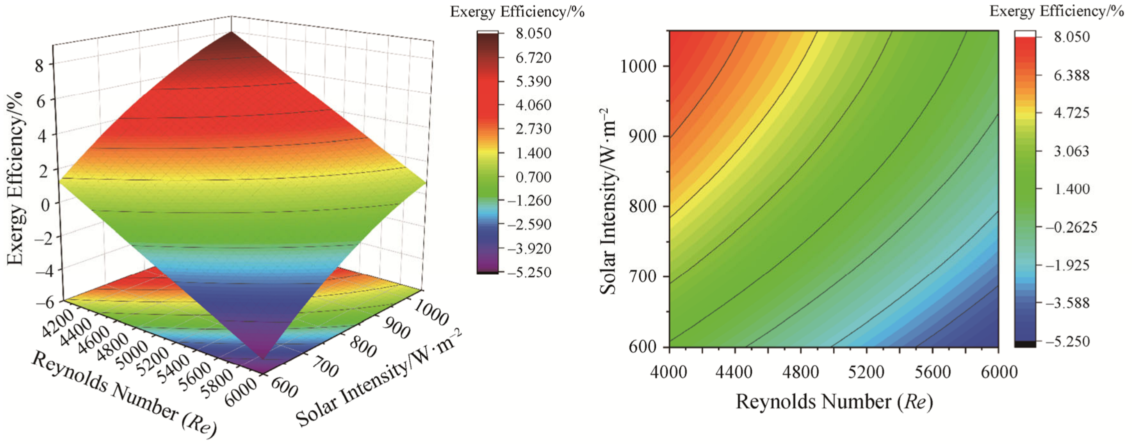

(a) Exergy efficiency variation with Reynolds Number and solar intensity

(b) Contour plot of exergy efficiency with Solar Intensity and Reynolds Number

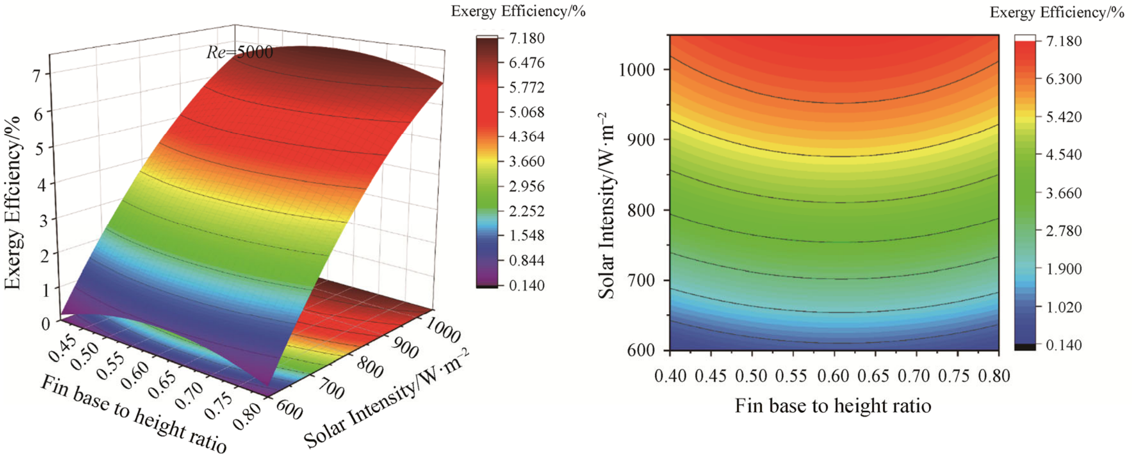

(c) Exergy efficiency with fin base to height ratio and solar intensity

(d) Exergy efficiency with Solar Intensity and fin base-to-height ratio

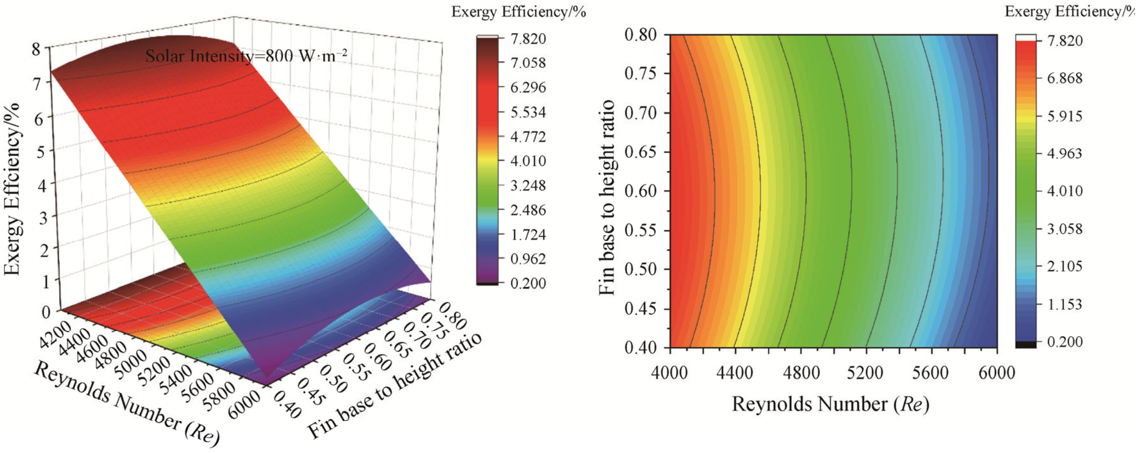

(e) Exergy efficiency variation with fin base to height ratio and Reynolds Number

(f) Contour plot of exergy efficiency with Reynolds Number and fin base-to-height ratio

Fig. 17 Exergy variation with input variables

12.10 Validation of response parameters with the Suresh et al. [38]

Fig. 23 shows the validation of responses Nusselt Number, THP, exergetic efficiency, and the friction factor with the Suresh et al. [38]. The results of the Nusselt number, THP, exergy efficiency, and friction factor are validated with good accuracy. Fig. 23(a) shows that maximum enhancement in Nusselt number is obtained at

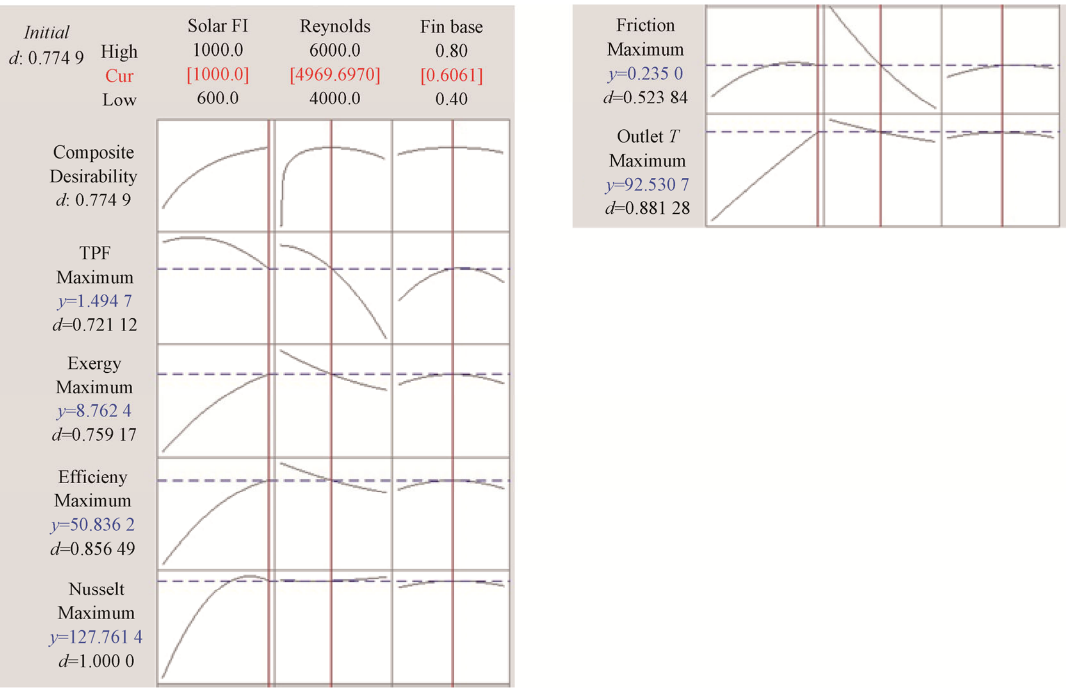

Fig. 18 Optimization plot of responses with input variables

Table 7 Validation of predicted results with experimental results

	Outlet Temperature /°C	Friction Factor f	Nusselt Number Nu	Efficiency η/%	Exergy efficiency η_{ex}/%	Thermal Performance factor TPF
RSM forecast results	92.53	0.2350	127.7614	50.83	8.7624	1.4927
Experimental results	89.087	0.2250	122.9064	48.24	8.4995	1.425
Error	3.72%	4.25%	3.8%	5.095%	3%	4.53%

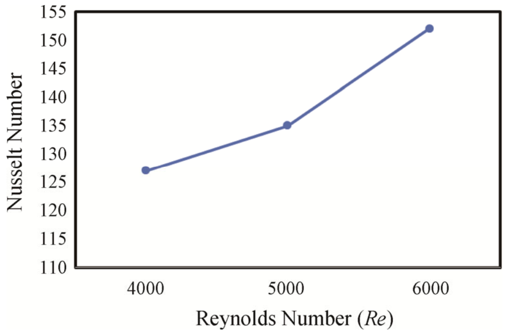

Fig. 19 Nusselt number variation with Reynolds number

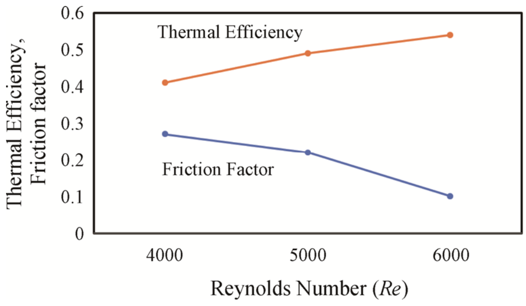

Fig. 20 Friction factor and thermal efficiency variation with Reynolds Number

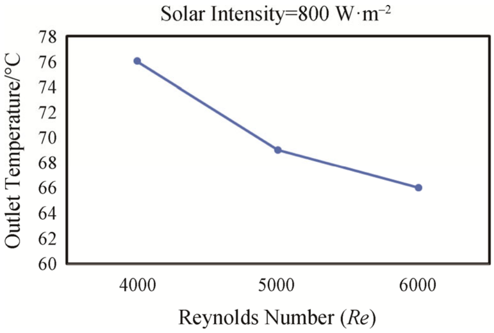

Fig. 21 Outlet temperature variation with the Reynolds number

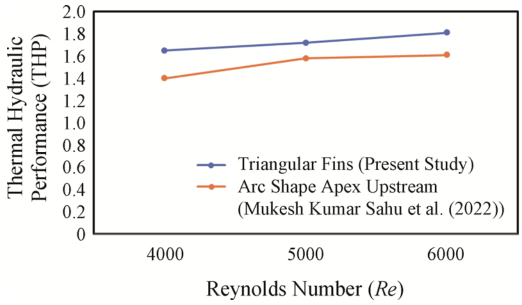

Fig. 22 Comparison of thermal-hydraulic performance with Arc shape apex upstream

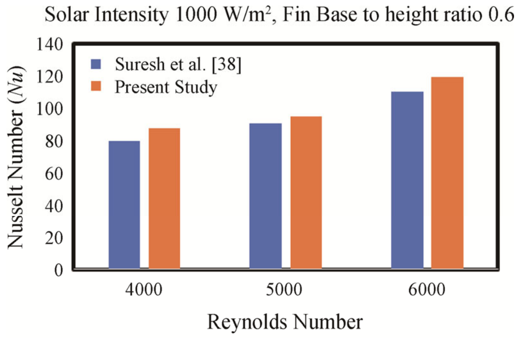

(a) Validation of Nusselt Number

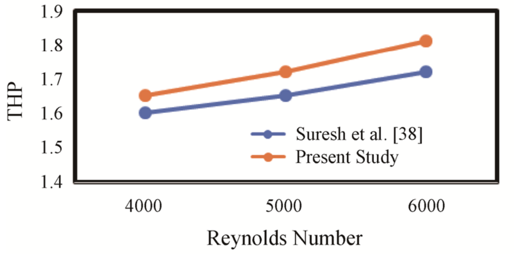

(b) Validation of THP

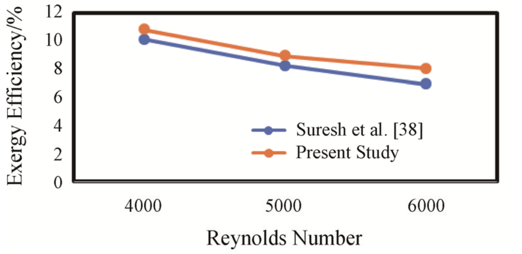

(c) Validation of Exegetic efficiency (%)

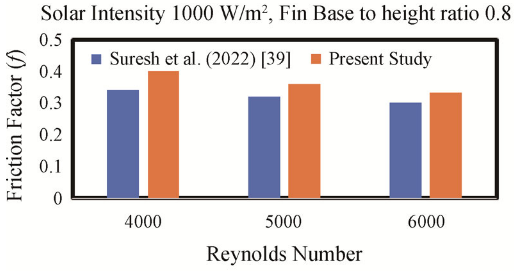

(d) Validation of Friction factor

Fig. 23 Validation of responses with the results in Suresh et al. [38]

Reynolds number of 6000. The maximum Nusselt numbers in Suresh et al. [38] and in the present study are 110 and 119, respectively. Fig. 23(b) represents the maximum enhancement in THP values in Suresh et al. [38] and the present study is 1.71 and 1.81 at Reynolds Number of 6000. The maximum exergetic efficiency in the present study and Suresh et al. [38] is found to be 10.78% and 10.1%, respectively at Reynolds number of 4000 in Fig. 23(c). Fig. 23(d) shows the higher values of the friction factor since the sudden stoppage of high-velocity air due to striking the face of fins. The maximum friction factor in the present study and the Suresh et al. [38] obtained to be 0.4 and 0.34 at Reynolds number of 4000.

13. Conclusions

This paper represents the analysis of finned solar air heaters. The main work targeted to optimizing the geometry of fins to maximize the heat transfer rate and minimize the blower pressure drops. For optimization purposes, the RSM tool is used. The RSM generates the performance parameters in the form of second order polynomial. The input variables selected are solar intensity, Reynolds number, and the fin base-to-height ratio. The following points have been concluded as the outcomes of this research.

(1) The solar intensity, Reynolds number, and the fin base to height ratio are three important parameters on which the performance of the SAH depends.

(2) The optimum solar intensity is 1000 W/m^2; Reynold number is 4969.67, and fin base to height 0.6061 which responses namely outlet temperature of 92.53°C, friction factor of 0.2350, Nusselt number of 127.7614, efficiency of 50.83%, exergy efficiency of 8.7624% and TPF of 1.4927.

(3) The optimum fin base-to-height ratio was found to be 0.6 which enhances the 7.56 times Nusselt number as compared to smooth surface. The increase in Reynolds Number increases the Nusselt Number but the exergy efficiency of the solar air heater is reduced. Due to the increase of Reynolds number, the pumping power increased which gives a negative effect on the exergy efficiency.

(4) The increased Reynolds number improves the turbulence and heat transfer to the air but also reduces the net efficiency of solar air heater due to increasing in pressure drop.

(5) The increased Reynolds number reduced the skin friction factor but simultaneously increased the form drag due to the striking of air on the face of the triangular surface, which increased the pressure drop.

(6) The predicted results and experimental results of responses are validated with error in outlet temperature of 3.72%, friction factor of 4.25%, Nusselt number of 3.8%, efficiency of 5.095%, exergy efficiency of 3%, and TPF of 4.53%.

(7) The composite desirability among input and output variables was found to be 77.46% which shows the good matching between the input and out variables.

(8) The standardized effect of all the response parameters was found to be 2.571 in which solar intensity is highly affected the system performance as compared to Reynolds number and the fin base to height ratio.

(9) The accuracy of the models has been tested by

ANOVA analysis in terms of S, $R^{2,}$ and R^2(adj) values. The maximum values of the S, $R^{2,}$ and R^2(adj) values were found to be 1.73, 99.73%, and 99.24%.

14. Future Scope

The solar air heater is very useful for heating the air with the help of solar energy. In the future, it gains popularity due to multiple uses like heating the room, crop drying, refineries, and wood seasoning plant. The various designs of solar air heaters have been developed and tested for finding the best optimum geometry. The selection of the optimum geometry is done based on the thermal-hydraulic performance parameters since the increase in roughness enhances both heat transfer and pressure drop simultaneously. In all designs of solar air heaters, we observe one common problem which is the reduction of the turbulence at the side wall of the solar air heater. So, our future work is focused on the generation of turbulence on the wall of the SAH. This can be achieved by reducing the width of the SAH, which has been maintained near 1 m in most of the design. In the present study, the main cause of pressure drop is the sudden stopping of the high-velocity air due to striking the face of the fins. So, in future work, I cut the corners of the fins and give the small angle inclination with the direction of the velocity of air which reduce the pressure drop and increase the thermal-hydraulic performance parameters.

Conflict of Interest

On behalf of all authors, the corresponding author states that there is no conflict of interest.

References

[1] Bauri K.S., Prasad K.S., A CFD-based thermal analysis of solar air heater duct artificially roughened with ‘S’ shape ribs on absorber plate. AIP Conferece Proceeding, 2021, 2341: 030009. doi: 10.1063/5.0050359.

[2] Xiao H., Wang J., Liu Z., Liu W., Turbulent heat transfer optimization for solar air heater with variation method based on exergy destruction minimization principle. International Journal of Heat and Mass Transfer, 2019, 136: 1096–1105. doi: 10.1016/J.IJHEATMASSTRANSFER.2019.03.071.

[3] Altfeld K., Leiner W., Fiebig M., Second law optimization of flat-plate solar air heaters Part I: The concept of net exergy flow and the modeling of solar air heaters. Solar Energy, 1988, 41(2): 127–132. DOI: 10.1016/0038-092X(88)90128-4.

[4] Mohanty P.C., Behura K.A., Singh R.M., et al., Parametric performance optimization of three sides roughened solar air heater. Energy Sources, Part A: Recovery, Utilization, and Environmental Effects, 2020, 43(18): 2319–2338. doi: 10.1080/15567036.2020.1752855.

[5] Mahanand Y., Senapati R.J., Thermo-hydraulic performance analysis of a solar air heater (SAH) with quarter-circular ribs on the absorber plate: A comparative study. International Journal of Thermal Science, 2021, 161(1): 106747. DOI: 10.1016/J.IJTHERMALSCI.2020.106747.

[6] Acır A., Canlı E.M., Ata I., Çakıroğlu R., Parametric optimization of energy and exergy analyses of a novel solar air heater with grey relational analysis. Applied Thermal Engineering, 2017, 122 (1): 330–338. DOI: 10.1016/J.APPLTHERMALENG.2017.05.018.

[7] Gill S.R., Hans S.V., Singh P.R., Optimization of artificial roughness parameters in a solar air heater duct roughened with hybrid ribs. Applied Thermal Engineering, 2021, 191(1): 116871. DOI: 10.1016/J.APPLTHERMALENG.2021.116871.

[8] Moradi R., Kianifar A., Wongwises S., Optimization of a solar air heater with phase change materials: Experimental and numerical study. Experimental Thermal Fluid Science, 2017, 89(1): 41–49. DOI: 10.1016/J.EXPTHERMFLUSCI.2017.07.011.

[9] Yadav S.A., Shrivastava V., Sharma A., Dwivedi K.M., Numerical simulation and CFD-based correlations for artificially roughened solar air heater. Materials Today Proceeding, 2021, 47(1): 2685–2693. DOI: 10.1016/J.MATPR.2021.02.759.

[10] Wang T., Zhao Y., Diao Y., et al., Experimental investigation of a novel thermal storage solar air heater (TSSAH) based on flat micro-heat pipe arrays. Renewable Energy, 2021, 173(1): 639–651. DOI: 10.1016/J.RENENE.2021.04.027.

[11] Sureandhar G., Srinivasan G., Muthukumar P., Senthilmurugan S., Performance analysis of arc rib fin embedded in a solar air heater. Thermal Science Engineering Progress, 2021, 23(3): 100891. DOI: 10.1016/J.TSEP.2021.100891.

[12] Kumar R., Goel V., Singh P., et al., Performance evaluation and optimization of solar assisted air heater with discrete multiple arc shaped ribs. Journal of Energy Storage, 2019, 26(1): 100978. DOI: 10.1016/J.EST.2019.100978.

[13] Parsa H., Saffar-Avval M., Hajmohammadi R.M., 3D simulation and parametric optimization of a solar air heater with a novel staggered cuboid baffles. International Journal of Mechanical Science, 2021, 205(2): 106607. DOI: 10.1016/J.IJMECSCI.2021.106607.

[14] Qader S.B., Supeni E.E., Ariffin A.K.M., et al., RSM

approach for modeling and optimization of designing parameters for inclined fins of solar air heater. Renewable Energy, 2019, 136: 48–68.
DOI: 10.1016/J.RENENE.2018.12.099.

[15] Benhamza A., Boubekri A., Atia A., et al., Multi-objective design optimization of solar air heater for food drying based on energy, exergy and improvement potential. Renewable Energy, 2021, 169: 1190–1209.
DOI: 10.1016/J.RENENE.2021.01.086.

[16] Salih M.M.M., Alomar R.O., Yassien S.N.H., Impacts of adding porous media on performance of double-pass solar air heater under natural and forced air circulation processes. International Journal of Mechanical Science, 2021, 210: 106738.
DOI: 10.1016/J.IJMECSCI.2021.106738.

[17] Abo-Elfadl S., Yousef S.M., El-Dosoky F.M., Hassan H., Energy, exergy, and economic analysis of tubular solar air heater with porous material: An experimental study. Applied Thermal Engineering, 2021, 196: 117294.

[18] Matheswaran M.M., Arjunan V.T., Muthusami T., et al., A case study on thermo-hydraulic performance of jet plate solar air heater using response surface methodology. Case Studies in Thermal Engineering, 2022, 34: 101983.
DOI: 10.1016/j.csite.2022.101983.

[19] Zulkifle I., Alwaeli A.H.A., Ruslan H.M., et al., Numerical investigation of V-groove air-collector performance with changing cover in Bangi, Malaysia. Case Studies Thermal Engineering, 2018, 12: 587–599.
DOI: 10.1016/J.CSITE.2018.07.012.

[20] Aboueian J., Shahsavar A., Feasibility study of improving the energy and exergy performance of a concentrating photovoltaic/thermal system by the simultaneous application of biological water-silver nanofluid and sheet-and-grooved tube collector: Two-phase mixture model. Engineering Analysis with Boundry Element, 2022, 144: 433–440.
DOI: 10.1016/J.ENGANABOUND.2022.08.039.

[21] Al-Damook M., Obaid A.H.Z., Qubeissi A.M., et al., CFD modeling and performance evaluation of multipass solar air heaters. Numerical Heat Transfer Part A: Applications, 2019, 76: 1–27.

[22] Gawande B.V., Dhoble S.A., Zodpe B.D., Chamoli S., Experimental and CFD investigation of convection heat transfer in solar air heater with reverse L-shaped ribs. Solar Energy, 2016, 131: 275–295.
doi: 10.1016/j.solener.2016.02.040.

[23] Yadav S.A., Bhagoria L.J., Heat transfer and fluid flow analysis of solar air heater: A review of CFD approach. Renewable and Sustainable Energy Reviews, 2013, 23: 60–79. DOI: 10.1016/j.rser.2013.02.035.

[24] Khanlari A., Sözen A., Tuncer D.A., et al., Numerical and experimental analysis of longitudinal tubular solar air heaters made from plastic and metal waste materials. Heat Transfer Research, 2021, 52(10): 19–45.
DOI: 10.1615/HEATTRANSRES.2021038204.

[25] Yadav S.A., Bhagoria L.J., A CFD (computational fluid dynamics) based heat transfer and fluid flow analysis of a solar air heater provided with circular transverse wire rib roughness on the absorber plate. Energy, 2013, 55: 1127–1142. DOI: 10.1016/J.ENERGY.2013.03.066.

[26] Sun W., Ji J., He W., Influence of channel depth on the performance of solar air heaters. Energy, 2010, 35: 4201–4207. DOI: 10.1016/j.energy.2010.07.006.

[27] Singh P.A., Singh P.O., Performance enhancement of a curved solar air heater using CFD. Solar Energy, 2022, 174: 556–569. DOI: 10.1016/j.solener.2018.09.053.

[28] Mahanand Y., Senapati R.J., Thermo-hydraulic performance analysis of a solar air heater (SAH) with quarter-circular ribs on the absorber plate: A comparative study. International Journal of Thermal Science, 2021, 161: 106747.
DOI: 10.1016/J.IJTHERMALSCI.2020.106747.

[29] Yadav S.A., Shrivastava V., Sharma A., Dwivedi K.M., Numerical simulation and CFD-based correlations for artificially roughened solar air heater. Materials Today Proceeding, 2021, 47: 2685–2693.
DOI: 10.1016/J.MATPR.2021.02.759.

[30] Sahu K.M., Prasad K.R., Exergy based performance evaluation of solar air heater with arc-shaped wire roughened absorber plate. Renewable Energy, 2016, 96: 233–243. DOI: 10.1016/j.renene.2016.04.083.

[31] Singh S., Dhiman P., Thermal and thermohydraulic performance evaluation of a novel type double pass packed bed solar air heater under external recycle using an analytical and RSM (response surface methodology) combined approach. Energy, 2014, 72: 344–359.
DOI: 10.1016/j.energy.2014.05.044.

[32] Azadani N.L., Gharouni N., Multi objective optimization of cylindrical shape roughness parameters in a solar air heater. Renewable Energy, 2021, 179: 1156–1168. DOI: 10.1016/j.renene.2021.07.084.

[33] Huddar B.V., Razak A., Cuce E., et al., Thermal performance study of solar air dryers for cashew kernel: a comparative analysis and modelling using Response Surface Methodology (RSM) and Artificial Neural Network (ANN). International Journal Photoenergy, 2022, pp: 4598921. DOI: 10.1155/2022/4598921.

[34] Çengel A.Y., Ghajar J.A., Kanoğlu M., Heat and mass transfer, fifth ed., Tata Magrahil, 2014 .

[35] Sobamowo G.M., Oguntala A.G., Yinusa A.A., Adedibu O. A., Analysis of transient heat transfer in a longitudinal fin with functionally graded material in the presence of magnetic field using finite difference method. World Scientific News, 2019, 137: 166–187.

[36] Han Y.M., Cho J.S., Kang H.S., Analysis of a one-dimensional fin using the analytic method and the finite difference method. Journal of the Korean Society for Industrial and Applied Mathematics, 2005, 9(1): 91–98.

[37] Peng H.S., Chen C.L., Hybrid differential transformation and finite difference method to annular fin with temperature-dependent thermal conductivity. International Journal of Heat and Mass Transfer, 2011, 54(11–12): 2427–2433. DOI: 10.1016/J.IJHEATMASSTRANSFER.2011.02.019.

[38] Gogada S., Roy S., Gupta A., et al., Energy and exergy analysis of solar air heater with trapezoidal ribs based absorber: A comparative analysis. Energy Science Engineering, 2023, 11(2): 585–605. DOI: 10.1002/ESE3.1347.

[39] Webb L.R., Eckert G.R.E., Application of rough surfaces to heat exchanger design. International Journal of Heat Mass Transfer, 1972, 15(9): 1647–1658. DOI: 10.1016/0017-9310(72)90095-6.

[40] Cortés A., Piacentini R., Improvement of the efficiency of a bare solar collector by means of turbulence promoters. Applied Energy, 1990, 36(4): 253–261. DOI: 10.1016/0306-2619(90)90001-T.

[41] Duffie A.J., Beckman A.W., Worek M.W., Solar engineering of thermal processes, 2nd ed., Solar Energy Engineering, 1994, 116(1): 67–68. DOI: 10.1115/1.2930068.

[42] Nayak K.J., Sukhatme P., Solar energy thermal collection and storage, third ed. Mcgraw-hill, India, 2010.

[43] Singh V., Yadav S.V., Optimizing the performance of solar panel cooling apparatus by application of response surface methodology. Proceedings of the Institution of Mechanical Engineers, Part C: Journal of Mechanical Engineering Science, 2022. DOI: 10.1177/09544062221101828.

[44] Singh V., Yadav S.V., Application of RSM to optimize solar pump LCOE and power output. IETE Journal of Research, 2022. DOI: 10.1080/03772063.2022.2069165.

[45] Sharma N., Choudhary R., Multi-objective performance optimization of a ribbed solar air heater. Energy Enviroment Sustainability, 2020, pp: 77–93. DOI: 10.1007/978-981-15-0675-8_6.

[46] Singh V., Yadav S.V., Bhutto K.J., et al., Comparison of different designs of solar air heater with the simple solar heater of having reflecting mirrors. Proceeding of Institution of Mechanical Engineering Part C, 2023, 237(21): 5156–5173. DOI: 10.1177/09544062231158530.

[47] Sahu K.M., Gorai K.V., Saha C.B., Applications of extended surfaces for improvement in the performance of solar air heaters—a detailed systematic review. Enviroment Science. Pollution Research, 2023, 30: 54429–54447. DOI: 10.1007/s11356-023-26360-3.

[48] Sajawal M., Rehman U.T., Ali M.H., et al., Experimental thermal performance analysis of finned tube-phase change material based double pass solar air heater. Case Studies in Thermal Engineering, 2019, 15: 100543. DOI: 10.1016/J.CSITE.2019.100543.

[49] Singh I., Vardhan S., Experimental investigation of an evacuated tube collector solar air heater with helical inserts. Renewale Energy, 2021, 163: 1963–1972. DOI: 10.1016/J.RENENE.2020.10.114.

[50] Manjunath S.M., Karanth V.K., Sharma Y.N., Numerical investigation on heat transfer enhancement of solar air heater using sinusoidal corrugations on absorber plate. International Journal of Mechanical Science, 2018, 138: 219–228. DOI: 10.1016/J.IJMECSCI.2018.01.037.

[51] Mesgar P.M., Heydari A., Wongwises S., Geometry optimization of double pass solar air heater with helical flow path. Solar Energy, 2021, 213: 67–80. DOI: 10.1016/J.SOLENER.2020.11.015.

[52] Ammar M., Mokni A., Mhiri H., Bournot P., Numerical analysis of solar air collector provided with rows of rectangular fins. Energy Reports, 2020, 6: 3412–3424. DOI: 10.1016/J.EGYR.2020.11.252.

[53] Sahu K.M., Kharub M., Matheswaran M.M., Nusselt number and friction factor correlation development for arc-shape apex upstream artificial roughness in solar air heater. Enviroment Science Pollution Research, 2022, 29(43): 65025–65042. DOI: 10.1007/s11356-022-20222-0.

[54] Sahu K.M., Sharma M., Matheswaran M.M., Maitra K., On the use of longitudinal fins to enhance the performance in rectangular duct of solar air heaters - a review. Journal of Solar Energy Engineering Transaction ASME, 2019, 141(3): 030802. DOI: 10.1115/1.4042827